14

JOURNAL OF APPLIED PHYSICS VOLUME 86, NUMBER 1 1998-1999 1 JULY 1999

Explicit Green's function of a boundary value problem for a sphere and trapped flux analysis in Gravity Probe B experiment

I. M. Nemenman[a] and A. S. Silbergleit
Gravity Probe B, W. W. Hansen Experimental Physics Laboratory, Stanford University, Stanford, California 94305-4085

(Received 25 January 1999; accepted for publication 1 April 1999)

Magnetic flux trapped on the surface of superconducting rotors of the Gravity Probe B (GP-B) experiment produces some signal in the superconducting quantum interference device readout. For the needs of GP-B error analysis and simulation of data reduction, this signal is calculated and analyzed in this article. We first solve a magnetostatic problem for a point source on the surface of a sphere, finding the closed form elementary expression for the corresponding Green's function. Second, we calculate the flux through the pick-up loop as a function of the source position. Next, the time dependence of a source position, caused by rotor motion according to a symmetric top model, and thus the time signature of its flux are determined, and the spectrum of the trapped flux signal is analyzed. Finally, a multipurpose program of trapped flux signal generation based on the above results is described, various examples of the signal obtained by means of this program are given, and their features are discussed. Signals of up to 100 fluxons, i.e., 100 pairs of positive and negative point sources, are examined.
[S0021-8979(99)08113-X]

I. INTRODUCTION

The Gravity Probe B (GP-B) satellite is scheduled to fly in the year 2000. It contains a set of gyroscopes intended to test the predictions of general relativity that a gyroscope in a low (altitude ≈650 km) circular polar orbit will precess, relative to a distant star, about 6.6 arcsec/year in the orbital plane (DeSitter, or geodetic, precession) and about 42 marcsec/year perpendicular to the orbital plane (Lense–Thirring, or frame-dragging, precession). To provide the desired measurement accuracy (1 part in 10^5 for the geodetic effect), a magnetic London moment readout using a superconducting quantum interference device (SQUID) has been chosen, so that the experiment will be carried out at low temperature (~2.5 K), and the gyrorotors will be superconducting (see Refs. 1, 2, and 3 for the design and status of the experiment; the history of GP-B development is found in Ref. 4, and a survey of space relativity tests is in Ref. 5). The direction of the magnetic London moment developed in a rotating superconductor coincides with the direction of the rotation (spin) axis[6] (for basic superconductor physics see Ref. 7; the description of gyromagnetic effects can be found in Ref. 8). The corresponding magnetic flux through the pick-up loop of the SQUID is proportional to the sine of the angle between the London moment vector and the pick-up loop plane, so the change of this angle, and thus the drift of the gyroscope axis, can be detected from the SQUID signal at the roll frequency of the spacecraft which will be deliberately rotated.

However, along with the London moment dipole, there will also be quantum-size sources of magnetic field pinned to the surface of the superconducting rotor (see Refs. 7 and 9). They appear in pairs of the opposite polarity called fluxons; the sources constituting the pair are connected by a magnetic vortex line going through the whole body of the superconductor (see Fig. 1). The fluxons produce additional magnetic flux through the pick-up loop called trapped flux; its time signature will be present in the SQUID output. The low frequency part of this signal, although comparatively small under the GP-B conditions, might corrupt the accuracy of the London moment readout. On the other hand, its high frequency part can provide additional information that is significant for the experimental results. To make sure the trapped flux does not affect the measurement precision, as well as to extract useful information from it, one has to analyze the trapped flux signal and develop the code generating it for the use in simulations of the GP-B error analysis and data reduction. This is the primary goal of the present article; we also hope that our analysis may be of use for other applications as well. Note that the first work on the analysis of the trapped flux from a GP-B rotor was done by Wai in his thesis.[10]

In Sec. II we give a closed form solution to a magnetostatic problem of a point field source (''magnetic charge,'' ''half-fluxon'') on the surface of the gyroscope. In Sec. III the solution is used to find the trapped flux signal in the pick-up loop as a function of the half-fluxon's position. The closed form expression for the trapped flux appears to be not very useful for further applications, so various exact and approximate formulas are also obtained. In Sec. IV we investigate the motion of fluxons with respect to the pick-up loop, thus finding the time signature of the trapped flux signal; we then go on to analyze its frequency spectrum. Section V contains a brief description of the program used to simulate

---

[a] Permanent address: Department of Physics, Princeton University, Princeton, NJ 08544; electronic mail: nemenman@princeton.edu

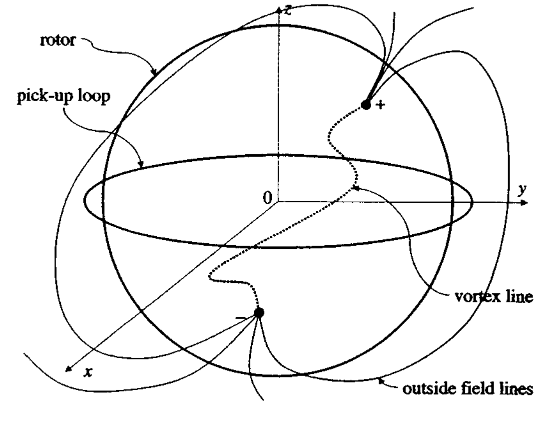

FIG. 1. Rotor with a fluxon.

trapped flux for the GP-B data processing routines. Pictures of the high frequency signal, its low frequency envelope, and various Fourier spectra are presented and discussed.

II. THE GREEN'S FUNCTION OF THE MAGNETOSTATIC PROBLEM

The GP-B experiment will be conducted at low temperatures, so the fluxons can be treated as static (welded to the rotor's surface) and noninteracting ones. In such a case the total fluxon field is a superposition of the fields of individual fluxons, each consisting of contributions from its positive and negative magnetic charges. In addition, the rate of change of this field due to the rotor's motion is negligible, hence the magnetostatic approach should be used. Thus we consider a single (positive) source of the field whose characteristic size is on the order of 10^{-5} cm;[9] due to a macroscopic size of the gyroscope (1.91 cm radius), this can be treated as a point source of magnetic field with the coordinate angles ϑ_+, φ_+ on the surface $r=r_g$ of the rotor. The spherical coordinates r, ϑ, φ here correspond to a Cartesian frame $\{x,y,z\}$ fastened to the pick-up loop so that the origin coincides with the loop center and the z axis is perpendicular to the loop plane; the real relative motion of the fluxon and the loop, i.e., the dependence of the position angles ϑ_+, φ_+ on time, will be incorporated and examined in Sec. IV.

In these settings, the boundary value problem for the magnetic potential $\Psi(\mathbf{r})$ of the fluxon outside the rotor is formulated as

$$\Delta\Psi(\mathbf{r})=0, \quad r>r_g, \; 0\leqslant\theta_+\leqslant\pi, \; 0\leqslant\varphi_+<2\pi, \tag{1}$$

$$-\left.\frac{\partial\Psi}{\partial r}\right|_{r=r_g}=\frac{\Phi_0}{r_g^2\sin\vartheta_+}\delta(\vartheta-\vartheta_+)\delta(\varphi-\varphi_+), \tag{2}$$

where $\Phi_0=h/2e$ is the magnetic flux quantum, and the magnetic field is

$$\mathbf{B}=-\nabla\Psi. \tag{3}$$

Evidently, up to a factor Φ_0, Ψ is the Green's function of the external Neumann boundary value problem for a sphere.

A standard separation of variables leads to the following series representation of the solution to Eqs. (1) and (2):

$$\Psi(\mathbf{r})\equiv\Psi(r,\vartheta,\varphi)=\frac{\Phi_0}{2\pi r_g}\sum_{l=0}^{\infty}\sum_{m=0}^{l}(M_{lm}\cos m\varphi + N_{lm}\sin m\varphi)\left(\frac{r_g}{r}\right)^{l+1}P_l^m(\cos\vartheta), \tag{4}$$

with the coefficients given by

$$M_{lm}=\frac{2l+1}{(1+\delta_{m0})(l+1)}\frac{(l-m)!}{(l+m)!}P_l^m(\cos\vartheta_+)\cos m\varphi_+,$$
$$N_{lm}=\frac{2l+1}{(l+1)}\frac{(l-m)!}{(l+m)!}P_n^m(\cos\vartheta_+)\sin m\varphi_+. \tag{5}$$

As it turns out, this series may be summed to give the closed form solution for Ψ. To determine it, we first introduce Eq. (5) into Eq. (4) to obtain

$$\Psi(\mathbf{r})=\frac{\Phi_0}{4\pi r_g}\sum_{l=0}^{\infty}\frac{2l+1}{l+1}\left(\frac{r_g}{r}\right)^{l+1}\left[P_l(\cos\vartheta)P_l(\cos\vartheta_+) + 2\sum_{m=0}^{l}P_l^m(\cos\vartheta)P_l^m(\cos\vartheta_+)\cos m(\varphi-\varphi_+)\right].$$

Then, by applying the addition theorem for Legendre functions [see Ref. 11 (10.11), (47)], we convert the latter into

$$\Psi(\mathbf{r})=\frac{\Phi_0}{4\pi r_g}\sum_{l=0}^{\infty}\frac{2l+1}{l+1}\left(\frac{r_g}{r}\right)^{l+1}P_l(\cos\gamma)$$
$$=\frac{\Phi_0}{4\pi r_g}\left[2\sum_{l=0}^{\infty}\left(\frac{r_g}{r}\right)^{l+1}P_l(\cos\gamma) - \sum_{l=0}^{\infty}\frac{1}{l+1}\left(\frac{r_g}{r}\right)^{l+1}P_l(\cos\gamma)\right], \tag{6}$$

where γ is the angle between the directions to the fluxon and to the observer

$$\cos\gamma\equiv\cos\vartheta\cos\vartheta_+ + \sin\vartheta\sin\vartheta_+\cos(\varphi-\varphi_+). \tag{7}$$

The first of the series in the above expression for Ψ is obviously the generating function for Legendre polynomials [see Ref. 11 (10.10), (39)], the second one is just an integral of it, namely,

$$\sum_{l=0}^{\infty}\frac{1}{l+1}\eta^{l+1}P_l(\zeta)=\int_0^{\eta}d\tau\sum_{l=0}^{\infty}\tau^l P_l(\zeta)$$
$$=\int_0^{\eta}\frac{d\tau}{\sqrt{1-2\zeta\tau+\tau^2}}$$
$$=\ln\frac{\eta-\zeta+\sqrt{1-2\zeta\eta+\eta^2}}{1-\zeta}.$$

Using these results in Eq. (6), we can now write the magnetic potential in its final form as a finite combination of elementary functions,

$$\Psi(\mathbf{r}) \equiv \Phi_0 G(\mathbf{r},\mathbf{r}_+) = \frac{\Phi_0}{2\pi}\left[\frac{1}{|\mathbf{r}-\mathbf{r}_+|} - \frac{1}{2r_g}\ln\frac{r_g^2-\mathbf{r}\cdot\mathbf{r}_+ + r_g|\mathbf{r}-\mathbf{r}_+|}{rr_g-\mathbf{r}\cdot\mathbf{r}_+}\right], \quad (8)$$

where $G(\mathbf{r},\mathbf{r}_+)$ is the Green function mentioned and $\mathbf{r}_+ = \{r_g, \vartheta_+, \varphi_+\}$ is the position vector of the source. The first term here, as one would expect, is a half of the potential of a point charge, and the addition to it describes the contribution of the curved boundary.

Since, surprisingly enough, we were not able to find this explicit formula in the literature, it seems reasonable to give here a closed form expression for the Green function of the corresponding Dirichlet problem (G_0), in which boundary condition (2) is replaced by

$$\Psi|_{r=r_g} = \frac{\Phi_0}{r_g \sin\vartheta_+}\delta(\vartheta-\vartheta_+)\delta(\varphi-\varphi_+). \quad (9)$$

The result then is

$$\Psi(\mathbf{r}) \equiv \Phi_0 G_0(\mathbf{r},\mathbf{r}_+) = \frac{\Phi_0}{4\pi}\frac{r^2-r_g^2}{|\mathbf{r}-\mathbf{r}_+|^3}. \quad (10)$$

Note that the Green's functions for the corresponding internal problems can be obtained from Eqs. (8) and (10) by means of inversion.

III. TRAPPED FLUX AS A FUNCTION OF A MAGNETIC CHARGE POSITION

Magnetic flux measured by the pick-up loop of a GP-B SQUID is the flux through the circle of the radius R in the plane $z=0$, or, equivalently, the flux through the (upper) hemisphere. The dependence of the trapped flux on the half-fluxon position turns out to be rather complicated, especially for the GP-B design, when the gap between the rotor and the loop is very small as compared to the pick-up loop radius R. For that reason we give here a number of different representations of the trapped flux as a function of the fluxon position; each of them has its own merits and drawbacks and is thus used for different purposes pertinent to our investigation.

A. Trapped flux in terms of a series of Legendre polynomials

The simplest way to calculate the trapped flux is to integrate over the hemisphere the series expression for the radial component of the magnetic field obtained from Eqs. (3)–(5):

$$\Phi_+ = \int_{\text{hemisphere } (r=R)} B_r\Big|_{r=R} dA = \int_{\text{hemisphere } (r=R)} -\frac{\partial\Psi}{\partial r}\Big|_{r=R} dA = \Phi_0\sum_{l=0}^{\infty}(l+1)\left(\frac{r_g}{R}\right)^l M_{l0}\int_0^1 P_l(s)\,ds;$$

all spherical harmonics with $m\neq 0$ here have averaged out over the azimuthal angle φ. The last integral is calculated with the help of the known relations of the theory of Legendre polynomials [see Ref. 11 (10.10), (14), (2), (4)]:

$$P_l(s) = \frac{P'_{l+1}(s)-P'_{l-1}(s)}{l+1}; \quad P_l(1)=1;$$

$$P_{2k+1}(0)=0; \quad P_{2k}(0) = \frac{(-1)^k}{\sqrt{\pi}}\frac{\Gamma(k+1/2)}{k!};$$

$$l,k=0,1,\dots;$$

$\Gamma(\zeta)$ is the Euler gamma function. Then, after inserting the values M_{l0} from Eq. (5), we arrive at the following expressions:

$$\Phi_+(\cos\vartheta_+) = \frac{\Phi_0}{2}F_\delta(\cos\vartheta_+);$$

$$F_\delta(s) = \sum_{k=0}^{\infty}(1-\delta)^{2k+1}P_{2k+1}(s)[P_{2k}(0)-P_{2k+2}(0)] = \frac{2}{\sqrt{\pi}}\sum_{k=0}^{\infty}(-1)^k\frac{k+3/4}{(k+1)!}\Gamma(k+1/2) \times(1-\delta)^{2k+1}P_{2k+1}(s). \quad (11)$$

Here δ denotes the dimensionless gap between the pick-up loop and the rotor, $0\leqslant\delta=(R-r_g)/R<1$.

From the point of view of signal processing, $F_\delta(s)$ is a transfer function which converts the "input" half-fluxon position signal $S_{\text{in}}(t)=\cos\vartheta_+(t)$ (the position is changing with time as the rotor moves relative to the pick-up loop; see Sec. IV), into an "output" trapped flux signal $S_{\text{out}}(t) = 0.5\Phi_0 F_\delta[S_{\text{in}}(t)]$ which is present in the GP-B readout. Since the total contribution to the flux of any number of fluxons scattered in any way over the rotor's surface is given by the sum of the values of the same function F_δ taken at proper different values of its argument, it was called "universal curve" in Ref. 10. Clearly, $F_\delta(s)$ is an odd function of s; in particular, $F_\delta(0)=0$ means that a source sitting exactly in the pick-up loop plane does not, of course, register any flux.

By setting $\delta=0$ in Eq. (11) (the loop on the surface of the rotor), we immediately find

$$F_0(s) = \frac{2}{\sqrt{\pi}}\sum_{k=0}^{\infty}(-1)^k\frac{k+3/4}{(k+1)!}\Gamma(k+1/2)P_{2k+1}(s) = \begin{cases} 1 & \text{if } 0<s\leqslant 1; \\ 0 & \text{if } s=0; \\ -1 & \text{if } -1\leqslant s<0 \end{cases} \quad (12)$$

(the last equality here is proved by expanding its right-hand side in the orthogonal series of Legendre polynomials).

This result obtained by Wai[10] has a clear physical meaning: when the pick-up loop lies on the rotor's surface, the same as the point source of field always does, the flux through the loop remains unchanged ($\pm\Phi_0/2$, half of the total) while the half-fluxon stays in either of the hemispheres separated by the plane of the loop, and changes its sign by a jump when the half-fluxon crosses this plane. However, Eq.

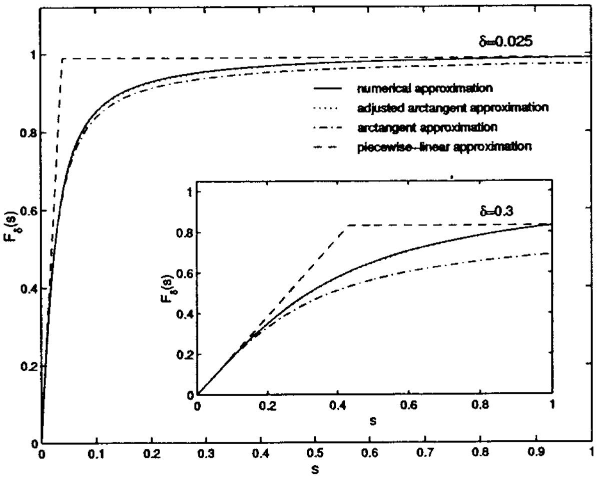

FIG. 2. Universal curve $F_\delta(s)$.

(12) also demonstrates the difficulties in using expression (11) for GP-B, where $\delta = 0.025$ is very small: for any $\delta > 0$ the series of Eq. (11) has an absolutely converging majorant, so its sum $F_\delta(s)$ is an analytical function of s, but it has a jump discontinuity at $s=0$ when $\delta = 0$. Therefore the series of Eq. (11) converges worse and worse with the separation δ becoming smaller and smaller, which makes Eq. (11) practically unacceptable for accurate numerical calculations at the required value of separation. It also turns finding *a uniform in s* asymptotic expansion of $F_\delta(s)$ for $\delta \to 0$ into a rather difficult mathematical problem. The effect is that for small positive values of δ the transfer function has the shape of a very steep "kink" [recall that $F_\delta(s)$ is odd]: it is almost constant outside a small vicinity $(-\Delta_\delta, \Delta_\delta)$ of the origin, with $\Delta_\delta = O(\delta)$ as shown below, and is equal to zero at $s=0$ with a huge gradient $\sim O(1/\delta)$ there (see Fig. 2). That is why we are deriving three more representations for $F_\delta(s)$ in the text that follows.

B. Integral representation of the trapped flux

An integral expression for $F_\delta(s)$ is obtained by replacing the Legendre polynomials in Eq. (11) by their integral representation [see Ref. 11 (10.10), (43)]

$$P_{2k+1}(\cos\vartheta_+) = \frac{1}{\pi}\int_{-\vartheta_+}^{\vartheta_+} \frac{\exp[i(2k+1+1/2)]\,d\psi}{\sqrt{2(\cos\psi - \cos\vartheta_+)}}.$$

Changing then the order of summation and integration, we arrive at a sum of two hypergeometric series which are readily summed up to result in

$$F_\delta(\cos\vartheta_+) = \frac{\Phi_0\sqrt{2}}{\pi}\int_0^{\vartheta_+} \frac{d\psi\exp(i\psi/2)}{\sqrt{\cos\psi - \cos\vartheta_+}} \times\left[\frac{\lambda}{\sqrt{1+\lambda^2}} - \frac{\sqrt{1+\lambda^2}}{2\lambda} + \frac{1}{2\lambda}\right], \tag{13}$$

$$\lambda \equiv (1-\delta)\exp(i\psi).$$

Representation (13) is very convenient for precise numerical calculation (and, in fact, is used for this purpose in our code; see Sec. V), because the integrand in Eqs. (13) is an algebraic one, and the weak singularity at the upper limit can be taken care of rather easily. The plot of the transfer function computed from Eqs. (13) is given in Fig. 2, along with graphs of its various approximations that are described in Sec. III C. The relative error of the numerical computation has been kept within 10^{-5}.

C. Elementary approximations of the trapped flux

From the described behavior of $F_\delta(s)$ for small δ it is clear that to effectively approximate it one needs the value of its gradient at $s=0$ and the "saturation" value $F_\delta(1)$ in the first place. Fortunately, it is possible to compute these quantities exactly, and they are

$$f_\delta \equiv F_\delta(1) = \frac{1}{1-\delta}\left[1 - \frac{2\delta - \delta^2}{\sqrt{1+(1-\delta)^2}}\right] = 1 - (\sqrt{2}-1)\delta + O(\delta^2); \tag{14}$$

$$\kappa_\delta \equiv \left.\frac{\partial F_\delta(s)}{\partial s}\right|_{s=0} = \frac{2}{\pi}\left[\frac{1+(1-\delta)^2}{1-(1-\delta)^2}\mathbf{E}(1-\delta) - \mathbf{K}(1-\delta)\right] = \frac{2}{\pi}\left[\frac{1}{\delta} + 2 + O(\delta\log\delta^{-1})\right], \quad \delta \to 0; \tag{15}$$

here $\mathbf{K}(k)$, $\mathbf{E}(k)$ are complete elliptic integrals of the first and second kind, respectively (see Ref. 14 for their definitions and asymptotic behavior at $k \to 1-0$). The formulas are derived from Eq. (11) by direct summation of the corresponding series of Legendre polynomials carried out in the Appendix.

The simplest approximation of the transfer function for $\delta \to +0$ is evidently a piecewise-linear one,

$$F_\delta(s) \approx \begin{cases} 1, & \text{if } \Delta_\delta < s \leq 1; \\ \kappa_\delta s, & \text{if } |s| \leq \Delta_\delta; \\ -1, & \text{if } -1 \leq s < -\Delta_\delta, \end{cases} \tag{16}$$

with Δ_δ defined in a natural way as

$$\kappa_\delta\Delta_\delta = f_\delta, \quad \Delta_\delta = \frac{f_\delta}{\kappa_\delta} = \frac{\pi}{2}\delta + O(\delta^2). \tag{17}$$

It turns out that this approximation gives the right qualitative picture of the signal and is even not too bad quantitatively, providing, for all values $|s| \leq 1$, the error within 1/3 for both $\delta = 0.3$ and $\delta = 0.025$. This accuracy, however, is not enough for the GP-B simulations; moreover, the largest error, associated with the jump of the derivative of function (16) at $s = \pm\Delta_\delta$, occurs in a very sensitive transition region where the fast growth of $F_\delta(s)$ is replaced by its almost constant behavior.

A much more attractive approximation is given by the function

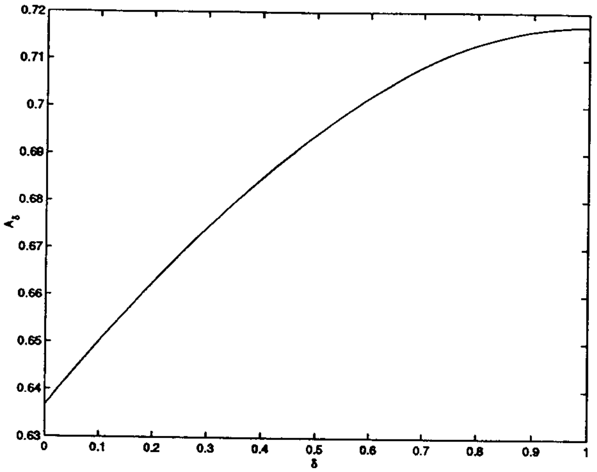

FIG. 3. Dependence of A_δ on δ.

$$F_\delta(s) \approx \frac{2}{\pi} f_\delta \arctan\left(\frac{\pi}{2}\frac{\kappa_\delta s}{f_\delta}\right), \quad \delta \to +0. \tag{18}$$

The parameters here are arranged in such a way that the slope at $s=0$ is exactly κ_δ and, in the spirit of asymptotic methods, the true saturation value is achieved when $\kappa_\delta s = \infty$ [note that another "simple and natural" approximating function, the hyperbolic tangent, is not acceptable, because the rate of approach of f_δ by $F_\delta(s)$ is a power rather than exponential one]. The performance of the approximation (18) exceeds all expectations, giving, over the whole range of s, a maximum error of 20% for $\delta=0.3$, and only 1.8% for $\delta=0.025$. The accuracy is mostly lost outside the transition zone $(-\Delta_\delta, \Delta_\delta)$ due to the fact that f_δ is achieved only at infinity. This can be dealt with by redefining the parameters to have both the exact slope at $s=0$ and the right value at $s=1$, which produces

$$F_\delta(s) \approx A_\delta \arctan\frac{\kappa_\delta s}{A_\delta}, \quad A_\delta \arctan\frac{\kappa_\delta}{A_\delta} = f_\delta, \quad \delta \to +0. \tag{19}$$

This "adjusted" arctan gives the maximum error within 0.3% for $\delta=0.025$; even for as large a separation as $\delta=0.3$ the error is still about 0.6%. Like in Eqs. (16) and (18), the dependence, Eq. (19), is shown in Fig. 2. Coefficient A_δ is plotted versus δ in Fig. 3; note the relative flatness of the function.

D. Closed form expression of the trapped flux

The explicit formula for the trapped flux can also be obtained, although not that easily, from Eq. (11); however, a direct way to get it is to integrate the closed form expression for the magnetic field through the pick-up loop plane $z=0$. For this plane $\vartheta=\pi/2$, $r=\rho$ (the polar radius); in addition, we can redefine φ by setting $\varphi_+=0$. Then Eqs. (8) and (3) provide the needed component of the magnetic field in the form

$$B_z|_{z=0} = -\frac{\Phi_0 r_g \cos\vartheta_+}{2\pi}\left[\frac{1}{X^3(\rho,\varphi)} + \frac{\rho - r_g \sin\vartheta_+ \cos\varphi}{2r_g^2 \rho X(\rho,\varphi)\, Y_+(\varphi)\, Y_-(\varphi)} + \frac{\sin\vartheta_+ \cos\varphi}{2r_g^2 \rho\, Y_+(\varphi)\, Y_-(\varphi)} - \frac{1}{2r_g^2 \rho\, Y_-(\varphi)}\right], \tag{20}$$

where

$$X(\rho,\varphi) = \sqrt{r_g^2 - 2r_g\rho \sin\vartheta_+ \cos\varphi + \rho^2},$$
$$Y_\pm(\varphi) = 1 \pm \sin\vartheta_+ \cos\varphi. \tag{21}$$

Now we need to integrate Eq. (20) over the area of the pick-up loop. First we calculate the simple, although rather cumbersome, algebraic integral of the field, Eq. (20), times $\rho d\rho$ over the polar radius from 0 to R (if instead, one first integrates over φ, elliptic integrals of a complicated argument appear in the result that make the closed form radial integration very difficult). As we are then to integrate over the period of $\cos\varphi$, the terms *odd* in $\cos\varphi$ can be omitted, and we obtain

$$\Phi_+(\cos\vartheta_+) = \frac{\Phi_0}{2} F_\delta(\cos\vartheta_+) = -\frac{\Phi_0 r_g \cos\vartheta_+}{2\pi} \times \int_0^{2\pi} d\varphi \left[\frac{R^2 - r_g^2}{2r_g^2 X(R,\varphi)\, Y_+(\varphi)\, Y_-(\varphi)} - \frac{R}{2r_g^2\, Y_-(\varphi)}\right]. \tag{22}$$

In view of Eqs. (21), this integration is also rather straightforward and leads to the desired result,

$$\Phi_+(\cos\vartheta_+) = \frac{\Phi_0}{2}\frac{\cos\vartheta_+}{1-\delta}\left\{\frac{1}{|\cos\vartheta_+|} - \frac{2\delta - \delta^2}{\pi\sqrt{2(1-\delta)(1+\sin\vartheta_+) + \delta^2}} \times \left[\frac{\mathbf{\Pi}(\nu_+, k)}{1+\sin\vartheta_+} + \frac{\mathbf{\Pi}(\nu_-, k)}{1-\sin\vartheta_+}\right]\right\}, \tag{23}$$

where

$$\nu_\pm(\vartheta_+) = \mp\frac{2\sin\vartheta_+}{1 \pm \sin\vartheta_+},$$
$$k(\vartheta_+, \delta) = \sqrt{\frac{4(1-\delta)\sin\vartheta_+}{2(1-\delta)(1+\sin\vartheta_+) + \delta^2}}, \tag{24}$$

and $\mathbf{\Pi}(\nu,k)$ is the complete elliptical integral of the third kind (see Ref. 14). As a consistency check, one may calculate the saturation value and the derivative at zero of the transfer function, Eq. (23), to see that they are indeed equal to the previously obtained values, Eqs. (14) and (15).

The first term in Eq. (23) evidently has a jump discontinuity at $s=\cos\vartheta_+=0$. Therefore, for all finite δ, the second term must contain the discontinuity of the opposite sign to make the sum of two analytical in s. Hence for small positive δ in the transition zone we are dealing with a small difference of two large quantities, which is always a problem.

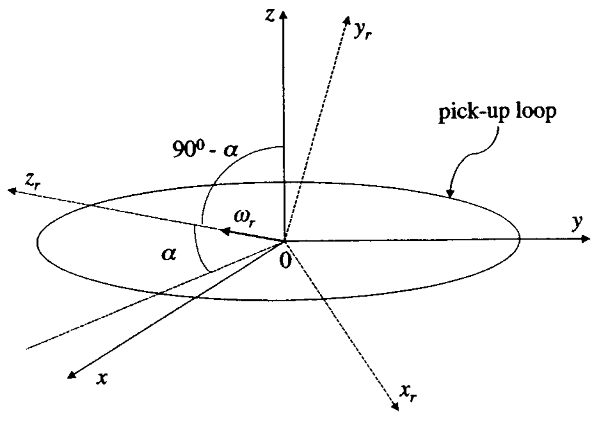

FIG. 4. Mutual orientation of roll and loop coordinates.

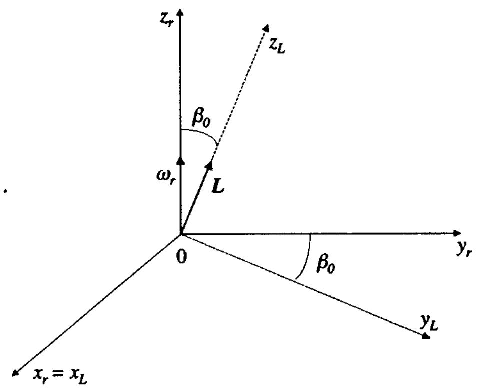

FIG. 5. Mutual orientation of roll and angular momentum coordinates.

Also, the first term in Eq. (23) coincides exactly with expression (12) for $\delta=0$, hence the second one should disappear in this limit, which it necessarily does in a very nonuniform way. Evidently, such an expression cannot be effectively used for both numerical and analytical purposes when δ is small enough, which is our case.

IV. FLUXON KINEMATICS AND SPECTRAL DECOMPOSITION OF THE TRAPPED FLUX SIGNAL

Now we need to determine the time signature $\vartheta_+(t)$ of a half-fluxon polar angle in the pick-up loop frame to complete investigation of the trapped flux signal.

In doing that we use four Cartesian coordinate systems. The first one $\{x, y, z\}$ has been introduced in Sec. I; it is fastened to the pick-up loop, and $\mathbf{z}$ is the unit vector normal to the loop plane (Fig. 1). The second coordinate system $\{x_r, y_r, z_r\}$ is associated with the roll axis of the spacecraft, $\hat{\omega}_r=\mathbf{z}_r$ (Fig. 4). The roll axis is almost in the pick-up loop plane, that is, the roll axis—pick-up loop plane misalignment $\alpha \leqslant 10^{-5}$ is very small. The third set of coordinates $\{x_L, y_L, z_L\}$ is related to the angular momentum vector $\mathbf{L}$ in a way that $\mathbf{z}_L=\mathbf{L}/|\mathbf{L}|$. Both the r and L coordinates are fixed in inertial space, since the roll axis is pointed to the Guide Star, and we can so far neglect the pointing errors, as well as the relativistic drift of $\mathbf{L}$. We choose axes $\mathbf{y}_r$ and $\mathbf{y}_L$ in the plane containing both $\mathbf{z}_r$ and $\mathbf{z}_L$, so then the perpendicular to this plane axes $\mathbf{x}_r$ and $\mathbf{x}_L$ coincides (Fig. 5), and the following relations are true:

$$\mathbf{z}_L\cdot\mathbf{z}_r=\mathbf{y}_L\cdot\mathbf{y}_r=\cos\beta_0,\quad \mathbf{z}_L\cdot\mathbf{y}_r=-\mathbf{y}_L\cdot\mathbf{z}_r=\sin\beta_0,$$
$$\mathbf{x}_r\cdot\mathbf{z}_r=\mathbf{x}_r\cdot\mathbf{z}_L=\mathbf{x}_r\cdot\mathbf{y}_r=\mathbf{x}_r\cdot\mathbf{y}_L=0. \tag{25}$$

Here β_0 is the roll axis—angular momentum misalignment which is required to be $\leqslant 5\times 10^{-5}$ rad in the GP-B experiment.

A symmetric top with the moment of inertia $I+\Delta I$ relative to the body symmetry axis and slightly different value I for the moments of inertia about the other two axes is a very good model for the GP-B rotors (note that $|\Delta I|/I \leqslant 10^{-5}$ for them). Therefore, we choose the fourth Cartesian coordinate system $\{x_B, y_B, z_B\}$ fixed in the rotor's body with $\mathbf{z}_B$ directed along the rotor's symmetry axis.

The dynamics of a symmetric rotor are well known and relatively simple (see Refs. 12 and 13). Its motion in the L coordinates is a precession about $\mathbf{z}_L$ with the spin frequency

$$\omega_s=\frac{L}{I}, \tag{26}$$

and rotation about the rotor symmetry axis $\mathbf{z}_B$ with the frequency

$$\omega_{\mathrm{rot}}=\frac{L}{I+\Delta I}\cos\gamma_B \simeq \omega_s\left(1-\frac{\Delta I}{I}\right)\cos\gamma_B\,; \tag{27}$$

$0\leqslant\gamma_B\leqslant\pi$ is the angle between $\mathbf{z}_L$ and $\mathbf{z}_B$.

For the signal of the trapped field we need, however, the time dependence of the position of a source in the inertial coordinates, hence we need expressions of $\mathbf{x}_B(t), \mathbf{y}_B(t), \mathbf{z}_B(t)$ in terms of $\mathbf{x}_L, \mathbf{y}_L, \mathbf{z}_L$. The latter is found with the help of the Euler angles (see, for instance, Ref. 12) in the form

$$\begin{aligned}
\mathbf{z}_B(t)&=\mathbf{z}_L\cos\gamma_B+\mathbf{x}_L\sin\gamma_B\cos\theta_s+\mathbf{y}_L\sin\gamma_B\sin\theta_s,\\
\mathbf{y}_B(t)&=-\mathbf{z}_L\sin\gamma_B\cos\theta_p\\
&\quad+\mathbf{x}_L(\cos\gamma_B\cos\theta_s\cos\theta_p-\sin\theta_s\sin\theta_p)\\
&\quad+\mathbf{y}_L(\cos\gamma_B\sin\theta_s\cos\theta_p+\cos\theta_s\sin\theta_p),\\
\mathbf{x}_B(t)&=-\mathbf{z}_L\sin\gamma_B\sin\theta_p\\
&\quad+\mathbf{x}_L(\cos\gamma_B\cos\theta_s\sin\theta_p+\sin\theta_s\cos\theta_p)\\
&\quad+\mathbf{y}_L(\cos\gamma_B\sin\theta_s\sin\theta_p-\cos\theta_s\cos\theta_p).
\end{aligned} \tag{28}$$

Here the spin and polhode phases are

$$\theta_s(t)=\omega_s t+\theta_s^0,\quad \theta_p(t)=\omega_p t+\theta_p^0,\quad \theta_{s,p}^0=\mathrm{const}, \tag{29}$$

and ω_p is a polhode frequency,

$$\omega_p=\frac{L}{I}\frac{|\Delta I|}{I}\cos\gamma_B=\omega_s\frac{|\Delta I|}{I}\cos\gamma_B \tag{30}$$

(in the body-fixed frame the instant angular velocity vector rotates around the rotor's symmetry axis with the polhode frequency). Using this, we obtain the following expression for the unit vector $\mathbf{e}_+$ in the direction of a half-fluxon (i.e., in the direction of an arbitrary fixed point of the rotor surface at some polar, $0 \leqslant \xi \leqslant \pi$, and azimuthal, $0 \leqslant \eta < 2\pi$, angles in the body-fixed spherical coordinates):

$$\begin{aligned}
\mathbf{e}_+ &= \mathbf{z}_B(t)\cos\xi + (\mathbf{x}_B(t)\cos\eta + \mathbf{y}_B(t)\sin\eta)\sin\xi \\
&\equiv e_1(t)\mathbf{x}_L + e_2(t)\mathbf{y}_L + e_3(t)\mathbf{z}_L, \\
e_1(t) &= \sin\xi[\cos\gamma_B\cos\theta_s(t)\sin(\theta_p(t)+\eta) \\
&\quad + \sin\theta_s(t)\cos(\theta_p(t)+\eta)] \\
&\quad + \cos\xi\sin\gamma_B\cos\theta_s(t), \\
e_2(t) &= \sin\xi[\cos\gamma_B\sin\theta_s(t)\sin(\theta_p(t)+\eta) \\
&\quad + \cos\theta_s(t)\cos(\theta_p(t)+\eta)] \\
&\quad + \cos\xi\sin\gamma_B\sin\theta_s(t) \\
e_3(t) &= -\sin\xi\sin\gamma_B\sin(\theta_p(t)+\eta) + \cos\xi\cos\gamma_B .
\end{aligned} \tag{31}$$

According to the results of Sec. III, we only need the cosine of the angle $\vartheta_+(t)$ between $\mathbf{e}_+(t)$ and the normal $\mathbf{z}(t)$ to the pick-up loop plane to study the trapped field signal; together with the loop, $\mathbf{z}(t)$ rotates about $\hat{\omega}_r$ with frequency ω_r (see Fig. 4):

$$\begin{aligned}
\mathbf{z}(t) &= \cos(\pi/2-\alpha)\hat{\omega}_r + \sin(\pi/2-\alpha)(\cos\theta_r\,\mathbf{x}_r + \sin\theta_r\,\mathbf{y}_r) \\
&\equiv \sin\alpha\,\mathbf{z}_r + \cos\alpha\,(\cos\theta_r\,\mathbf{x}_r + \sin\theta_r\,\mathbf{y}_r), \\
\theta_r &= \theta_r(t) = \omega_r t = \text{roll phase.}
\end{aligned} \tag{32}$$

By means of this, Eqs. (31), and formulas (25) relating the r and L coordinates to the first order in the misalignments β_0 and α we obtain (quadratic and higher order terms are several orders below the required GP-B accuracy):

$$\begin{aligned}
&\cos\vartheta_+(t) = a_{s-r}\sin\Theta_{s-r} + a(\beta_0\sin\theta_r + \alpha), \\
&\Theta_{s-r}(t) = (\omega_s-\omega_r)t + q_{s-r}; \quad \theta_r(t) = \omega_r t.
\end{aligned} \tag{33}$$

For a perfectly spherical rotor $\Delta I = 0$ and the amplitudes and initial phase here are true constants whose values depend only on the position of a fluxon relative to the symmetry axis, $a_{s-r} = \sin\xi$, $q_{s-r} = \eta$, $a = \cos\xi$. If, on the other hand, $\Delta I \neq 0$, they start to vary slowly with time at the polhode frequency according to

$$\begin{aligned}
a_{s-r}(\omega_p t) &= \sqrt{[\cos\xi\sin\gamma_B + \sin\xi\cos(\omega_p t + \theta_p^0 + \eta)]^2 + \sin^2\xi\cos^2\gamma_B\sin^2(\omega_p t + \theta_p^0 + \eta)}, \\
\tan q_{s-r}(\omega_p t) &= \frac{\sin\xi\cos\gamma_B\sin(\omega_p t + \theta_p^0 + \eta)}{\cos\xi\sin\gamma_B + \sin\xi\cos(\omega_p t + \theta_p^0 + \eta)}, \\
a(\omega_p t) &= \cos\xi\cos\gamma_B - \sin\xi\sin\gamma_B\sin(\omega_p t + \theta_p^0 + \eta).
\end{aligned} \tag{34}$$

Note that under the conditions of the GP-B experiment the spin frequency is always much larger than the roll and polhode ones, $\omega_r \sim 5\times10^{-5}\omega_s$, $\omega_p \sim 10^{-5}\omega_s$. Since generally the second term in the first equation of Eqs. (33) is about five orders of magnitude smaller than the first one, the input signal for the trapped flux output $\Phi_+(t) = (\Phi_0/2)F_\delta[\cos\vartheta_+(t)]$ is a single carrier harmonics of the (high) spin minus roll frequency (Θ_{s-r}), slowly modulated in the phase and amplitude at polhode frequency, added to by a small dc offset (αa) and a small low frequency harmonics (θ_r), both modulated at ω_p. Therefore it is natural and convenient to represent $\Phi_+(t)$ as a Fourier series of spin minus roll harmonics with the amplitudes modulated by low frequencies, namely,

$$\begin{aligned}
\Phi_+(t) &= \frac{\Phi_0}{2}F_\delta(\cos\vartheta_+(t)) \\
&= \frac{\Phi_0}{2}\Bigg[a_{s-r}(\omega_p t)\sum_{k=0}^{\infty}A_k(\omega_p t) \\
&\quad \times\sin(2k+1)\Theta_{s-r}(t) + a(\omega_p t)\,(\beta_0\sin\omega_r t + \alpha) \\
&\quad \times\sum_{k=0}^{\infty}B_k(\omega_p t)\cos 2k\Theta_{s-r}(t)\Bigg];
\end{aligned} \tag{35}$$

$$\begin{aligned}
A_k(\omega_p t) &= \frac{2}{\pi(2k+1)}\int_0^\pi \cos(2k+1)\psi\cos\psi \\
&\quad \times F'_\delta(a_{s-r}(\omega_p t)\sin\psi)\,d\psi + O(\beta_0^2); \\
B_k(\omega_p t) &= \frac{2}{\pi(1+\delta_{k0})}\int_0^\pi \cos 2k\psi \\
&\quad \times F'_\delta(a_{s-r}(\omega_p t)\sin\psi)\,d\psi + O(\beta_0^2);
\end{aligned}$$

here the prime denotes the derivative of $F_\delta(s)$ in s.

As readily seen, the amplitudes of *odd* harmonics of Θ_{s-r} (A_k) are generally of the order of unity and decrease as $O(k^{-2})$ for a large enough number k. In contrast with that, the amplitudes of *even* harmonics, which are linear in the misalignments, are at least four orders of magnitude smaller but decrease only as $O(k^{-1})$, $k\to\infty$. In addition, the even harmonics are modulated also by the roll frequency ω_r, so that, along with the harmonics $2k\Theta_{s-r}(t)$, $k = 0,1,\ldots$, with amplitudes $\alpha a_r(\omega_p t)B_k(\omega_p t)$, harmonics $2k\Theta_{s-r}(t) \pm \omega_r t$ are present, whose amplitudes differ only by the misalignment involved, $0.5\beta_0$ instead of α.

With all this in mind, one can easily understand that the full spectrum of the trapped flux signal consists of the following series of frequencies: $(2k+1)(\omega_s-\omega_r) \pm m\omega_p$, $2k(\omega_s-\omega_r) \pm \omega_r \pm m\omega_p$ and $2k(\omega_s-\omega_r) \pm m\omega_p$, m,k

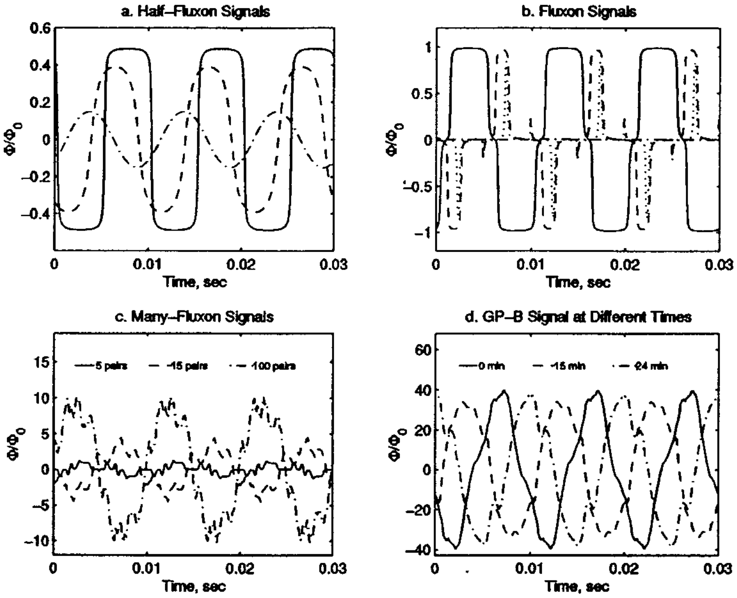

FIG. 6. Simulated readout signals.

$=0,1,\ldots$. The highest peaks are at $(2k+1)(\omega_s-\omega_r)$, and those at $2k(\omega_s-\omega_r)\pm\omega_r$ and $2k(\omega_s-\omega_r)$ are four to five orders of magnitude smaller. All of them are surrounded by an appropriately scaled forest of side bands separated by $\pm m\omega_p$.

The only remaining thing is to discuss briefly the total flux Φ produced by *all* fluxons. There are always some N fluxons present on the rotor's surface after cooling the rotor down below the transition temperature. Experiments have indicated that the expected number of the pairs is around $N \sim 100$, at most. We denote any values related to either positive or negative half-luxons by indexes + and −, respectively, numbering them with the index $i=1,2,\ldots,N$; for instance, their body coordinates will be ξ^i_+, η^i_+ and ξ^i_-, η^i_-, the input signals $S^i_+(t)=\cos\vartheta^i_+(t), S^i_-(t)=\cos\vartheta^i_-(t)$, etc.

The general expression for the total trapped field flux is given by

$$\Phi(t)=\sum_{i=0}^{N}\,[\Phi^i_+(t)+\Phi^i_-(t)]$$

$$=\frac{\Phi_0}{2}\sum_{i=0}^{N}\,[F_\delta(\cos\vartheta^i_+(t))-F_\delta(\cos\vartheta^i_-(t))]; \quad (36)$$

obviously, the full spectral representation of $\Phi(t)$ is just a scaled up version of $\Phi_+(t)$ given in Eqs. (35).

Since for small δ the transfer function $F_\delta(s)$ is close to $\pm F_\delta(1)\approx\pm1$ everywhere except within a small vicinity of the origin (see Sec. III), expressions (36) and (35) demonstrate that the maximum value of $\Phi(t)$ is distributed according to the usual counting statistics, provided that the distribution of fluxons over the surface of the rotor is a uniform random one. Therefore N fluxons in this case should produce a total flux on the order of $\sqrt{N}\Phi_0$ for "large" N.

V. CODE AND SIGNAL ANALYSIS

For the GP-B error analysis and data reduction one needs to simulate the trapped flux signal as expected in the SQUID output. To do that, the results obtained earlier were utilized for writing a program that is able to be fast enough to generate, store, and analyze the high-frequency signal. The code, written in the MATLAB V.5.0 to ensure compatibility with other GP-B software, is available from the authors.

The program is very versatile, allowing many options and many different tasks. For instance, there may be a different *number of fluxons*, and their *positions* may be read either from a prewritten file or generated at random according to different probability distributions. *Transfer function* may be calculated by means of several different expressions introduced in Sec. III. Generation of the *high frequency signal* and/or its slow varying *Fourier amplitudes*, Eqs. (35) and (36), is possible. In addition, all gyroscope and pick-up loop parameters (radii, rotor asphericity, misalignments, etc.), as well as the discretization frequency, time intervals, and all angular velocities may be specified in an arbitrary way.

A lot of attention in the program's realization has been paid to the fact that tracing positions of as much as 100 fluxons for long enough periods of time with high discretization frequency easily becomes too memory consuming. The program has thus been optimized in several directions, so as to not cause excessive memory swaps to the hard drive and not lead to the memory fragmentation, and to access the hard drive for data storage as infrequently as possible. The following data may be useful to estimate the code's speed: on a Sun UltraSparc 5 with 128 megabytes of random access memory (RAM) running System V, Rel. 4.0 and having a network mounted storage drive it takes, depending on the network load, from 1.5 up to 2 h to generate 1 h of signal of

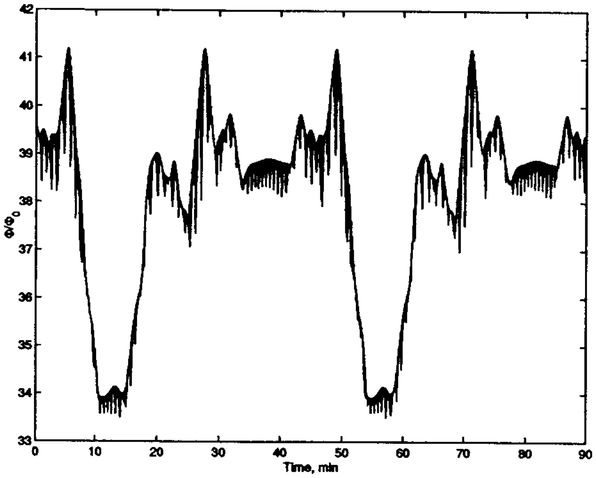

FIG. 7. Envelope of the simulated trapped flux signal, $T_p \approx 43.6$ min.

100 fluxons at a sampling frequency of 2200 Hz (the actual sampling rate of GP-B electronics).

We will not elaborate more here on the code details but will continue with the results of our simulations. All of them have been performed with the parameters set at the values expected for the GP-B experiment (see cf. Refs. 1–3). In particular, the spin frequency $f_{\text{spin}} = 100$ Hz, the roll period $T_r = 3$ min, the polhode period $T_p \approx 43.6$ min; recall that $\delta = 0.025$.

In Fig. 6 the signals are seen as generated by different number of fluxons distributed in various ways over the surface of the gyroscope. In all of the graphs the "adjusted arctan" approximation (19) to the universal curve is used. Figure 6(a) shows signals of a positive half-fluxon (without its negative counterpart) positioned at different points on the gyro. The majority of magnetic charge positions provide signals like the one drawn as a solid line. The dashed and dash-dotted lines correspond to rare charges oscillating in a small ($\sim \Delta_\delta$) vicinity of the pick-up loop plane, which is why their amplitude is smaller. On average, one cannot expect too many charges like that, however, each of the four GP-B rotors will carry just one *particular* realization of the fluxon position distribution, so these "weak" half-fluxons are possible.

Figure 6(b) shows various signals from one fluxon. Again, the solid line corresponds to "the most probable" signal: the positive and negative half-fluxons are far from each other (although not opposite on the sphere) and have large oscillation amplitudes.

Figure 6(c) shows typical signals of 5, 15, and 100 fluxons distributed *randomly* with the *uniform* probability over the gyro's surface. The $\sqrt{N}$ growth of the signal is visible; the complexity of the signal profile also clearly increases with N.

Figure 6(d) shows short fragments of the 12 h of signal generated for the test of the GP-B data reduction algorithms. There are 100 fluxons distributed unevenly: 60 of them are uniformly spread at random over the surface [just like in Fig. 6(c)], while the remaining 40 are used to create a total net flux of $\sim 40\,\Phi_0$ along some random axis. This should account for the small residual magnetization of the rotor at the time when it was made superconducting (see Ref. 17). This magnetization not only significantly increases the amplitude of the signal, it also smoothes it out. Different curves in Fig. 6 correspond to the signals taken at different stages of the polhoidal motion (namely, 0, 15, and 24 min from some reference point) for a duration of three spin periods.

In Fig. 7 a low-frequency envelope is plotted of the signal from Fig. 6(d) used in the GP-B simulations. The graph was constructed by splitting the magnetic flux signal into 2 s blocks (4400 data points in each) and plotting the maximum value of the flux for each block. The periodicity of the large scale structures of the envelope with an approximate polhode period of about 43 min is clear. On the other hand, a comparison of the signal in any two corresponding regions demonstrates that the short scale features, presumably introduced by the roll frequency and other less intensive harmonics, are not repeated precisely every polhode period T_p, which is expected because T_p and the roll period T_r are incommensurable.

Figure 8 shows the slow polhoidal variation of Fourier amplitudes of the spin minus roll harmonics calculated according to Eqs. (35) and summed over the fluxons. The first 10 odd and even harmonics are shown in plots (a) and (b), respectively, in Fig. 8. Recall that in expressions (35) for the flux all even harmonics are multiplied by the misalignments, so that the actual vertical scale in Fig. 8(b) is about 10^5 that in Fig. 8(a). The pictures clearly show that the odd harmon-

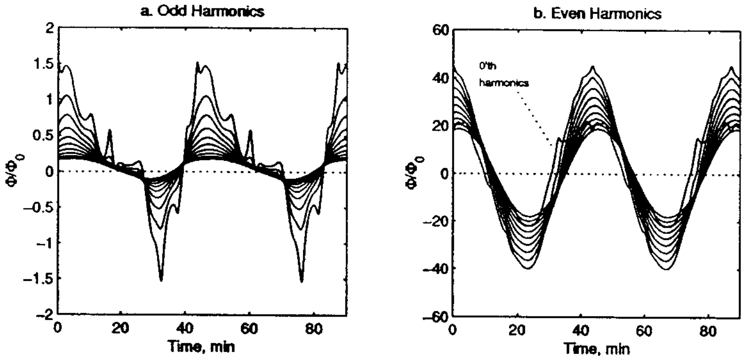

FIG. 8. Slowly varying amplitudes of the Fourier harmonics of the trapped flux signal, $T_p \approx 43.6$ min.

ics drop much faster with the number than the even ones, as predicted. It is interesting to note that the lowest even ($n=0$) harmonics, which gives the amplitude of the dc and the roll frequency components, has a shape rather distinctive from the profile of the other modes.

ACKNOWLEDGMENTS

This work was supported by NASA Grant No. NAS 8-39225 to Gravity Probe B. The authors are grateful to Dr. G. M. Keiser, who had originally initiated this work, Dr. M. Heifetz for many valuable comments, and to the Gravity Probe B Theory group for fruitful discussions.

APPENDIX: SUMMATION OF CERTAIN SERIES OF LEGENDRE POLYNOMIALS

Here we give a derivation of formulas (14) and (15) for $f_\delta = F_\delta(1)$ and for the slope κ_δ of the transfer function at $s=0$. We use the Pochgammer symbol $(\alpha)_0 = 1$, $(\alpha)_k = \alpha(\alpha+1)\ldots(\alpha+k-1) = \Gamma(\alpha+k)/\Gamma(\alpha)$, as well as the standard notation,

$$F(a,b,c;\zeta) = \sum_{k=o}^{\infty} \frac{(a)_k (b_k)}{(c)_k} \frac{\zeta^k}{k!},$$

for the Gauss hypergeometric function of argument ζ and parameters a, b, and c. From Eq. (11) we have

$$\begin{aligned} F_\delta(s) &\equiv F_\delta^{(1)}(s) - F_\delta^{(2)}(s); \\ F_\delta^{(1)}(s) &= 2\eta \sum_{k=0}^{\infty} \frac{(-\eta^2)^k}{k!} \left(\frac{1}{2}\right)_k P_{2k+1}(s), \qquad \text{(A1)} \\ F_\delta^{(2)}(s) &= \frac{\eta}{2} \sum_{k=0}^{\infty} \frac{(-\eta^2)^k}{(k+1)!} \left(\frac{1}{2}\right)_k P_{2k+1}(s), \end{aligned}$$

where we introduced $\eta = 1-\delta$ for brevity.

A. Calculation of f_δ

Since $P_n(1) = 1$, we have

$$F_\delta^{(1)}(1) = 2\eta \sum_{k=0}^{\infty} \frac{(-\eta^2)^k}{k!} \left(\frac{1}{2}\right)_k = \frac{2\eta}{\sqrt{1+\eta^2}};$$

$$F_\delta^{(1)}(1) = \frac{\eta}{2} \sum_{k=0}^{\infty} \frac{(-\eta^2)^k}{(k+1)!} \frac{(\frac{1}{2})_k (1)_k}{(2)_k} = \frac{\eta}{2} F(1/2, 1, 2; -\eta^2) = \eta^{-1}(\sqrt{1+\eta^2} - 1),$$

and for the elementary expression of the hypergeometric function we have used formula (11) from Ref. 15 (2.11) with $a=1/2$ and $b=1$. Combining these results with Eqs. (A1), we obtain

$$\begin{aligned} f_\delta &= F_\delta(s) = F_\delta^{(1)}(s) - F_\delta^{(2)}(s) \\ &= \frac{2\eta}{\sqrt{1+\eta^2}} - \frac{\sqrt{1+\eta^2} - 1}{\eta} = \frac{1}{\eta}\left(1 - \frac{1-\eta^2}{\sqrt{1+\eta^2}}\right), \end{aligned}$$

which, in view of $\eta = 1-\delta$, is exactly the same as expression (14).

B. Calculation of κ_δ

As [see Ref. 15 (10.10), (12)]

$$P'_{2k+1}(0) = (2k+1)\, P_{2k}(0) = \frac{(-1)^k}{k!} \left(\frac{3}{2}\right)_k,$$

from Eqs. (A1) we find

$$\begin{aligned} \left.\frac{\partial F_\delta^{(1)}}{\partial s}\right|_{s=0} &= 2\eta \sum_{k=0}^{\infty} \frac{(-\eta^2)^k}{k!} \left(\frac{1}{2}\right)_k P'_{2k+1}(0) \\ &= 2\eta \sum_{k=0}^{\infty} \frac{(\eta^2)^k}{k!} \frac{(\frac{1}{2})_k (\frac{3}{2})_k}{(1)_k} \\ &= 2\eta\, F(1/2, 3/2, 1; \eta^2) \qquad \text{(A2)} \\ &= \frac{2\eta}{1-\eta^2} F(1/2, -1/2, 1; \eta^2) \\ &= \frac{4\eta}{\pi(1-\eta^2)} \mathbf{E}(\eta), \end{aligned}$$

where $\mathbf{E}(\eta)$ is the complete elliptical integral of the second kind, and we have exploited the classical relation [see Ref. 15 (2.1.4), (23)]

$$F(a,b,c;\zeta) = (1-\zeta)^{c-a-b} F(c-a, c-b, c; \zeta),$$

and the expression for the elliptical integral in terms of the hypergeometric function [see Ref. 16 (13.8)] is

$$F(1/2, -1/2, 1; \eta^2) = \frac{2}{\pi} \mathbf{E}(\eta). \qquad \text{(A3)}$$

Similarly,

$$\begin{aligned} \left.\frac{\partial F_\delta^{(2)}}{\partial s}\right|_{s=0} &= \frac{\eta}{2} \sum_{k=0}^{\infty} \frac{(-\eta^2)^k}{(k+1)!} \left(\frac{1}{2}\right)_k P'_{2k+1}(0) \\ &= \frac{\eta}{2} \sum_{k=0}^{\infty} \frac{(\eta^2)^k}{k!} \frac{(\frac{1}{2})_k (\frac{3}{2})_k}{(2)_k} \\ &= \frac{\eta}{2} F(1/2, 3/2, 2; \eta^2) \\ &= \frac{\eta}{2}(-4) \frac{d}{d(\eta^2)} F(-1/2, 1/2, 1; \eta^2) \\ &= \frac{-4\eta}{\pi} \frac{d}{d(\eta^2)} \mathbf{E}(\eta) = -\frac{2}{\pi\eta}[\mathbf{E}(\eta) - \mathbf{K}(\eta)], \end{aligned} \qquad \text{(A4)}$$

and here we used the formula for the derivative of the hypergeometric function [see Ref. 15 (2.8), (20)], formula (A3) again, and a formula for the derivative of $\mathbf{E}(\eta)$ [see Ref. 16 (13.7), (12)]; $\mathbf{K}(\eta)$ is the complete elliptic integral of the first kind.

Equations (A2) and (A4) now provide

$$\kappa_\delta=\left.\frac{\partial F_\delta}{\partial s}\right|_{s=0}=\left.\frac{\partial F_\delta^{(1)}}{\partial s}\right|_{s=0}-\left.\frac{\partial F_\delta^{(2)}}{\partial s}\right|_{s=0}$$

$$=\frac{2}{\pi\eta}\left[\frac{1+\eta^2}{1-\eta^2}\mathbf{E}(\eta)-\mathbf{K}(\eta)\right],$$

which coincides with the exact expression in Eq. (15); the asymptotic formula there for small $\delta=1-\eta$ is obtained by using the expansions of elliptical integrals in the series in the conjugate modulus [see Ref. 14 (773.3), (774.3)].

[1] J. P. Turneaure *et al.*, Adv. Space Res. 9, 29 (1989).

[2] S. Buchman *et al.*, in *Proceedings of the 7th Marcel Grossman Meeting on General Relativity*, edited by R. T. Jantzen and G. M. Keiser (World Scientific, Singapore, 1996), Part B, p. 1533.

[3] B. Muhlfelder *et al.* in Ref. 2, p. 1545.

[4] C. W. F. Everitt, in *Near Zero*, edited by J. D. Fairbank, B. S. Deaver, Jr., C. W. F. Everitt, and P. F. Michelson (Freeman, New York, 1988), p. 685.

[5] G. M. Keiser, in Ref. 2, p. 207.

[6] F. London, *Superfluids* (Dover, New York, 1961), Vol. 1.

[7] M. Tinkham, *Introduction to Superconductivity* (McGraw–Hill, New York, 1996), Chaps. 5.

[8] L. Landau and E. Lifshitz, *Electrodynamics of Continuous Media*, 2nd ed. (Pergamon, Oxford, 1984), Chap. 4.

[9] A. C. Rose-Innes and E. H. Rhoderick, *Introduction to Superconductivity* (Pergamon, Oxford, 1978), Chap. 12.

[10] L. L. Wai, BS honors thesis, Dept. of Physics, Stanford University, 1989.

[11] H. Bateman and A. Erdélyi, *Higher Transcendental Functions*, (McGraw–Hill, New York, 1953), Vol. 2.

[12] L. Landau and E. Lifshitz, *Mechanics* (Pergamon, Oxford, 1959).

[13] H. Goldstein, *Classical Mechanics* (Addison–Wesley, Reading, MA, 1950).

[14] H. B. Dwight, *Tables of Integrals and Other Mathematical Data*, 4th ed. (Macmillan, New York, 1961), Chap. IX.

[15] H. Bateman and A. Erdélyi, in Ref. 11, Vol. 1.

[16] H. Bateman and A. Erdélyi, in Ref. 11, Vol. 3.

[17] G. T. Haupt, Ph.D. thesis, Dept. of Aeronautics and Astronautics, Stanford University, 1989.

1999

GPS Receiver Satellite/Antenna Selection Algorithm for the Stanford Gravity Probe B Relativity Mission

Jie Li, *Stanford University*
Awele Ndili, *Stanford University*
Lisa Ward, *Ball Aerospace & Technologies Corporation*
Saps Buchman, *Stanford University*

BIOGRAPHY

Jie Li, Ph.D., is a visiting scholar in the Gravity Probe B Relativity Mission at Stanford University. He received his Ph.D. degree from the Chinese Academy of Space Technology in Beijing, P. R. China.

Awele Ndili, Ph.D., is the project manager for GPS receiver development for the Gravity Probe B Relativity Mission at Stanford University. He received his Ph.D. and M.S. degrees from Stanford University. He has been working on GPS systems since 1992.

Lisa Ward, Ph.D., was the former project manager for GPS receiver development for the Gravity Probe B Relativity Mission at Stanford University. She received her Ph.D. degree from University of Colorado.

Saps Buchman, Ph.D., is the payload electronics manager for the Gravity Probe B Relativity Mission at Stanford University. He received his Ph.D. degree in physics from Harvard University.

ABSTRACT

This paper presents a GPS receiver satellite/antenna selection algorithm for the Stanford Gravity Probe B Relativity Mission. A Trimble Advanced Navigation Sensor Vector receiver onboard the space vehicle, a four-antenna six-channel GPS receiver, will provide real-time navigation solutions for orbit trim and raw measurements for ground post-processing, both for more accurate position and velocity and for attitude solutions. The GPS receiver satellite/antenna selection algorithm will determine the visibility of GPS satellites and assign a satellite and a master antenna to each receiver channel in order to maintain signal tracking. In this paper a new four-step GPS satellite selection algorithm is presented, which shows good performance with much less computations compared to the conventional algorithms. The smooth transfer between subsequent GPS satellite sets is also considered in the algorithm, such that continuity of the navigation data is maintained. The antenna selection algorithm is designed to maximize the signal to noise ratio of each master antenna. This paper also presents simulation results of performance comparisons of this new algorithm with conventional algorithms.

INTRODUCTION

The Stanford Gravity Probe B Relativity Mission is a space experiment designed to test Einstein's theory of General Relativity [1]. The Gravity Probe B space vehicle (GP-B) will operate in a polar, circular orbit at the altitude of 650 km, and will roll in the direction of a guide star with a period ranging from 1 minute to 3 minutes. A Trimble Advanced Navigation Sensor (TANS) Vector receiver onboard GP-B, a four-antenna six-channel GPS receiver developed by Trimble Navigation Ltd., will provide real-time navigation solutions for orbit trim and raw measurements for ground post-processing, both for more accurate position and velocity and for attitude solutions.

Previous papers [2] and [3] presented the design of the GPS receiver for the Stanford Gravity Probe B Relativity Mission and the prototypical development efforts including verification test plan and its preliminary results. Compared to the work described in [2] and [3], there are two major changes: (1) The Trimble TANS Vector receiver is used instead of the Loral Tensor receiver; (2) GPS attitude solutions will not be used onboard GP-B, but used for cross-checking on the ground.

With its four antennas, the TANS Vector receiver can track up to six GPS satellites, one on each channel. The RF-signals from four antennas are time-multiplexed, and a switch sequentially feeds the output signal of each antenna into all six channels. One antenna is assigned as the master antenna for each channel, which provides the signal used for code and carrier tracking, while the other three antennas provide differential phase measurements, referenced to the master antenna. The designation of master antenna can vary from channel to channel, and it can also vary from time to time for each channel.

Fig.1 illustrates the GP-B space vehicle and the GPS antenna configuration. GP-B has a science telescope pointed at an inertially fixed guide star and rolls about its pointing axis at the rate of 0.33~1 rpm. The four antennas are aligned in different directions, such that continuous visibility of GPS satellites will be maintained while GP-B rolls. The forward antennas 1 and 2 are 45° apart from the bore-sight axis of the telescope, and the aft antennas 3 and 4 are 135° apart from it. Antennas 1 and 2 are perpendicular to one another and out of phase by 180°, and so are antennas 3 and 4. The aft set is out of phase by 90° from the forward set. GPS receivers have never been flown in this configuration before, and it presents a challenge to the software design.

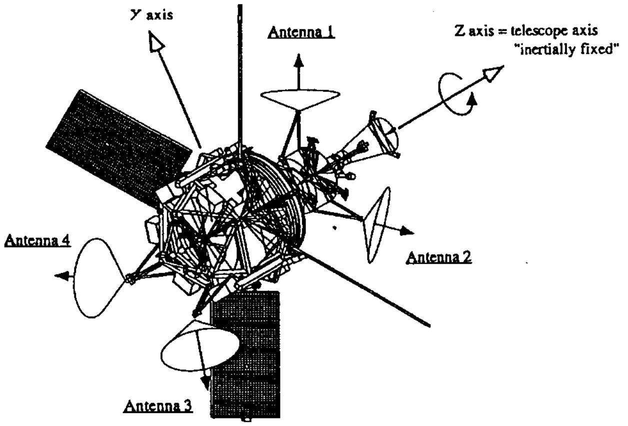

Fig.1 GP-B space vehicle and GPS antenna configuration

The GPS receiver satellite/antenna selection algorithm will determine the visibility of GPS satellites and assign a satellite and a master antenna to each receiver channel in order to maintain signal tracking. The general purpose of the GPS satellite selection algorithm is to minimize the Geometric Dilution Of Precision(GDOP) to improve the position accuracy. However, minimum GDOP algorithms tend to be computationally intensive, while some computationally simpler algorithms have poor GDOP performance. In this paper a new GPS satellite selection algorithm is presented, which shows good performance with much less computations compared to conventional algorithms. The smooth transfer between subsequent GPS satellite sets is also considered in the algorithm, such that continuity of the navigation data is maintained. The antenna selection algorithm is designed to maximize the Signal-to-Noise-Ratio (SNR) of the master antenna.

This paper is organized as follows: First, several coordinate systems are defined. Then the field-of-view (FOV) of antennas is analyzed. The GPS satellite and the antenna selection algorithm are presented separately, and some simulation results are given to compare the performance of this new algorithm with conventional algorithms. Finally, conclusions are derived.

COORDINATE SYSTEMS

As illustrated in Fig.2, several coordinate systems are defined.

Earth-centered inertial coordinate system: O_I is at the center of the Earth, $\vec{Z}_I$ is in the direction of the north pole, $\vec{X}_I$ is perpendicular to $\vec{Z}_I$ and fixed in an inertial direction, and $\vec{Y}_I$ completes the right-handed triad.

Body-centered inertial coordinate system: O_B is at the mass center of GP-B, $\vec{Z}_R$ is in the direction of the guide star, $\vec{X}_R$ lies in the orbital plane of GP-B and makes an acute angle with the direction of the north pole, and $\vec{Y}_R$ completes the right-handed triad.

Body-centered body-fixed coordinate system: O_B is at the mass center of GP-B, $\vec{Z}_B$ is aligned in the bore-sight axis of the science telescope, $\vec{X}_B$ and $\vec{Y}_B$ are fixed to the body of GP-B and complete the right-handed triad.

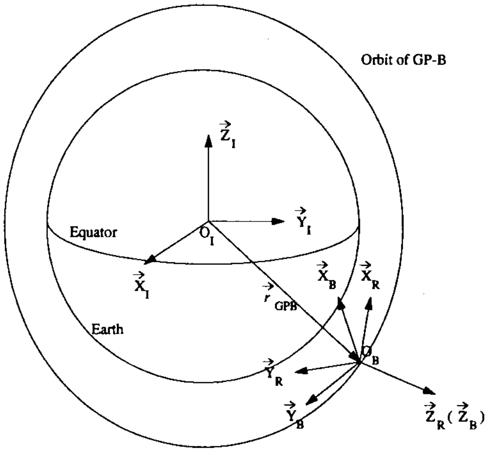

Fig.2 Coordinate systems

FIELD-OF-VIEW OF ANTENNAS

The four antennas are aligned in different directions. The nominal azimuth and elevation angles of the four antennas are given in Table 1, and the components of the pointing axes in $O_B - \vec{X}_B\vec{Y}_B\vec{Z}_B$ are

$$Va_{1-B} = \begin{bmatrix} 0 & \sqrt{2}/2 & \sqrt{2}/2 \end{bmatrix}^T \quad (1)$$

$$Va_{2-B} = \begin{bmatrix} 0 & -\sqrt{2}/2 & \sqrt{2}/2 \end{bmatrix}^T \quad (2)$$

$$Va_{3-B} = \begin{bmatrix} \sqrt{2}/2 & 0 & -\sqrt{2}/2 \end{bmatrix}^T \quad (3)$$

$$Va_{4-B} = \begin{bmatrix} -\sqrt{2}/2 & 0 & -\sqrt{2}/2 \end{bmatrix}^T \quad (4)$$

	Azimuth angle	Elevation angle
Antenna 1	90°	45°
Antenna 2	270°	45°
Antenna 3	0°	-45°
Antenna 4	180°	-45°

Table 1. Azimuth and elevation angles of antennas

Fig.3 shows the FOV of four antennas separately in $O_B - \vec{X}_B\vec{Y}_B\vec{Z}_B$. The ellipses are traces with same antenna elevation angles, which are 10°, 20° ..., 80° from the outer to inner ellipses. Two factors are considered in the analysis of FOV of GPS antennas: (1) A mask angle is used to specify the antenna elevation angle below which GPS satellites cannot be tracked on the antenna. The nominal value of the mask angle is 10°. (2) The FOV of the antenna is also obstructed by some structural parts of GP-B, such as the sunshade and solar arrays.

Fig.4 shows the combined FOV of four antennas. The lines denote the edges of the FOV for each antenna. Since the FOVs for the antennas overlap, the numbers in each area denote which antennas share that portion of the view. It is clear that the combined FOV of the four antennas covers the entire sky with a solid angle of 4π steradian. Any GPS satellite visible to GP-B is located in the FOV of at least 1 antenna, and at most 3. So the GPS satellite/antenna selection algorithm can be divided into two independent steps: (1) Select six satellites from all GPS satellites visible to GP-B and assign them to six channels; (2) Assign a master antenna to each channel to maintain visibility of the GPS satellite.

SATELLITE SELECTION ALGORITHM

Geometry of GPS satellites with minimum GDOP

The GDOP describes the general relationship between the errors in the pseudo-range measurements by the GPS receiver to the user position accuracy. In order to improve the GPS-based positioning accuracy, the GPS satellite selection algorithm should minimize GDOP of the selected GPS satellites.

From the almanacs of GPS satellites, the components of the position vector of a GPS satellite j (j=1, ..., 32) in $O_I - \vec{X}_I\vec{Y}_I\vec{Z}_I$ can be determined, which is denoted as r_{j-I}. Based on orbit parameters of GP-B, the components of its position vector in $O_I - \vec{X}_I\vec{Y}_I\vec{Z}_I$ can also be determined, which is denoted as r_{GPB-I}. So the unit vector pointing from GP-B to the GPS satellite j is $e_{j-I} = (r_{j-I} - r_{GPB-I}) / \left| r_{j-I} - r_{GPB-I} \right|$, where $\left| r_{j-I} - r_{GPB-I} \right|$ is the magnitude of $r_{j-I} - r_{GPB-I}$.

Signals from four GPS satellites are required to determine the 3-dimensional position and the user clock bias. Suppose the four GPS satellites are indexed as *j1, j2, j3, j4*, the GDOP is given as follows:

$$GDOP(j1, j2, j3, j4) = tr[(G^T G)^{-1}] \quad (5)$$

where

$$G = \begin{bmatrix} e_{j1-I,x} & e_{j1-I,y} & e_{j1-I,z} & 1 \\ e_{j2-I,x} & e_{j2-I,y} & e_{j2-I,z} & 1 \\ e_{j3-I,x} & e_{j3-I,y} & e_{j3-I,z} & 1 \\ e_{j4-I,x} & e_{j4-I,y} & e_{j4-I,z} & 1 \end{bmatrix} \quad (6)$$

The geometry of four satellites with minimum GDOP is illustrated in Fig.5, where one satellite A is at the zenith, and the other three satellites B, C and D are all equally spaced at 120°, and placed 109.47° apart from A to provide a regular tetrahedron[4, 5]. The minimum GDOP is 1.5811.

Define a coordinate system: O_a is at the position of the user, $\vec{Z}_a$ is in the direction of satellite A, $\vec{X}_a$ is perpendicular to $\vec{Z}_a$ and has satellite B in the plane $O_a - \vec{Z}_a\vec{X}_a$, and $\vec{Y}_a$ completes the right-handed triad. The components of direction vectors of four satellites are

$$V_A = \begin{bmatrix} 0 & 0 & 1 \end{bmatrix}^T \quad (7)$$

$$V_B = \begin{bmatrix} 2\sqrt{2}/3 & 0 & -1/3 \end{bmatrix}^T \quad (8)$$

$$V_C = \begin{bmatrix} -\sqrt{2}/3 & \sqrt{6}/3 & -1/3 \end{bmatrix}^T \quad (9)$$

$$V_D = \begin{bmatrix} -\sqrt{2}/3 & -\sqrt{6}/3 & -1/3 \end{bmatrix}^T \quad (10)$$

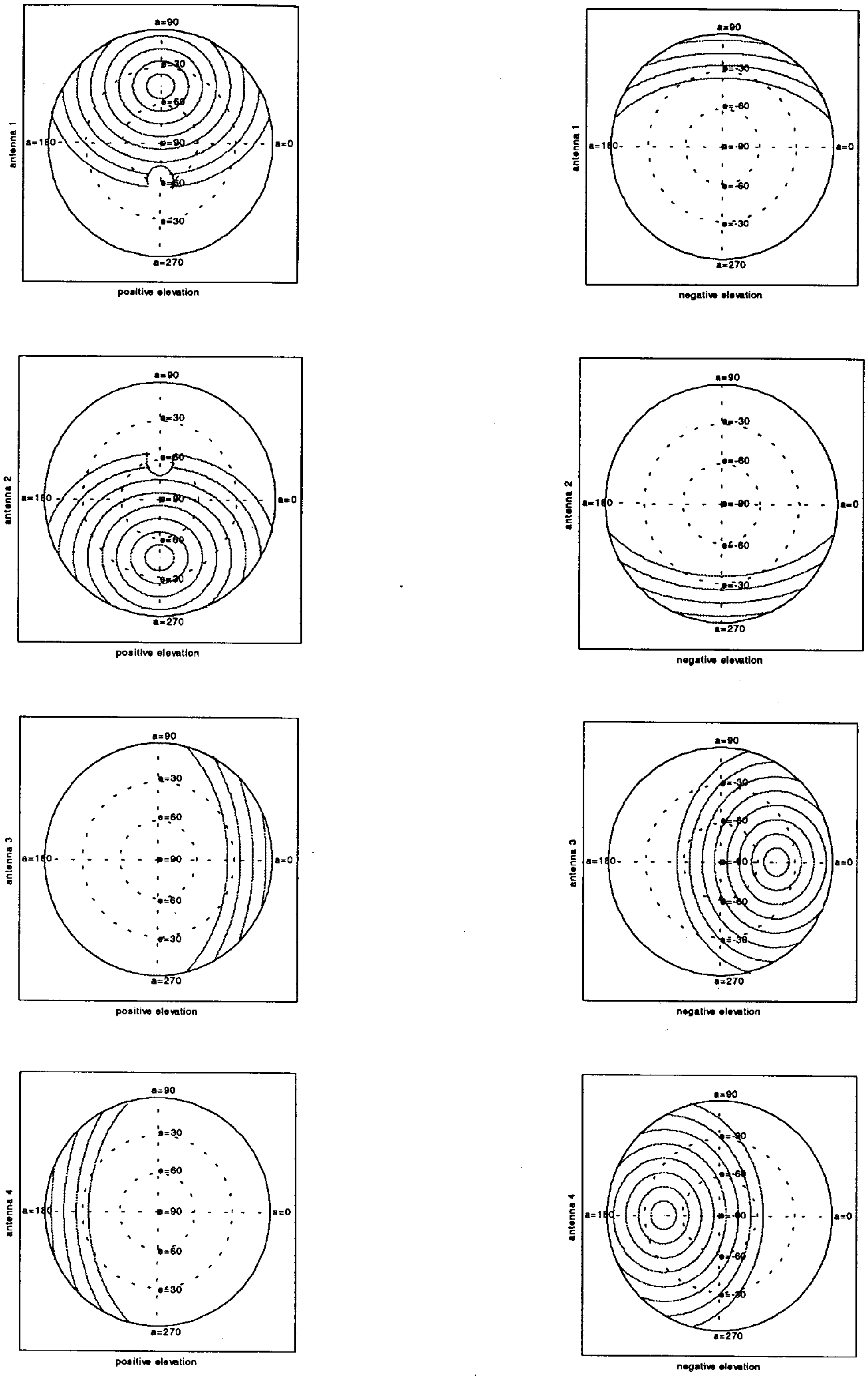

Fig. 3 Field-of-view of antennas

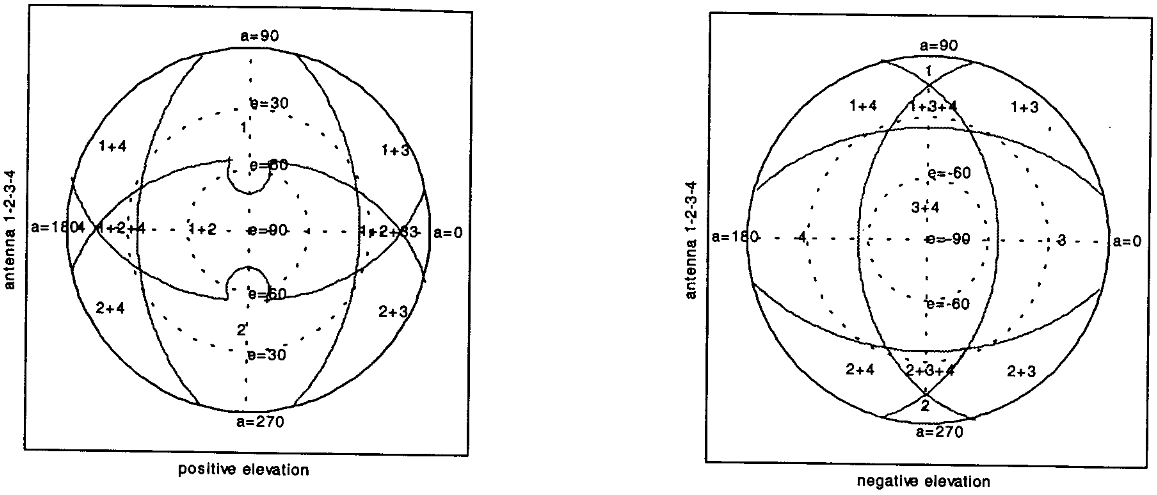

Fig.4 Combined field-of-view of four antennas

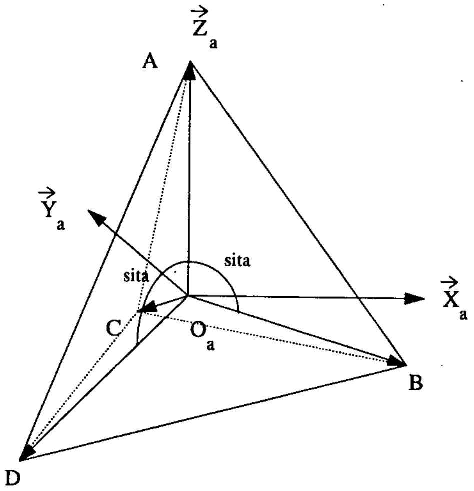

Fig.5 Geometry of GPS satellites with minimum GDOP

Visibility of GPS satellites

The GPS satellites are selected from the satellites visible to GP-B, i.e. the vector pointing from GP-B to the GPS satellite should be above the shell of the Earth occultation.

Let β_j be the angle between the unit vector e_{j-I} and the unit vector of the GP-B position e_{GPB-I}, then the GPS satellite j is visible when the following condition is satisfied

$$\cos(\beta_j) = (e_{j-I})^T e_{GPB-I} > \cos\gamma_{oc} \qquad (11)$$

where γ_{oc} is the threshold angle of the Earth occultation.

Considering the smooth transfer between the subsequent GPS satellite sets (which will be discussed later), it is also required that the selection at time t_n should be made from the satellites which are visible in the time period $[t_n - \Delta t_{up},\ t_n + \Delta t_{up}]$, where Δt_{up} is the update period of the GPS satellite selection algorithm. This gives the GPS receiver time to acquire and track the GPS satellite before using it for the computation of a solution.

Simulations are carried out to study the visibility of GPS satellites with the nominal GP-B orbit parameters and GPS almanacs. Fig.6 illustrates the number of visible GPS satellites in a simulation for a period of 12 hours, where the update period is 1 minute. It is shown that the minimum and maximum number of the visible GPS satellites are 9 and 15 respectively, and the mean number is 11.8.

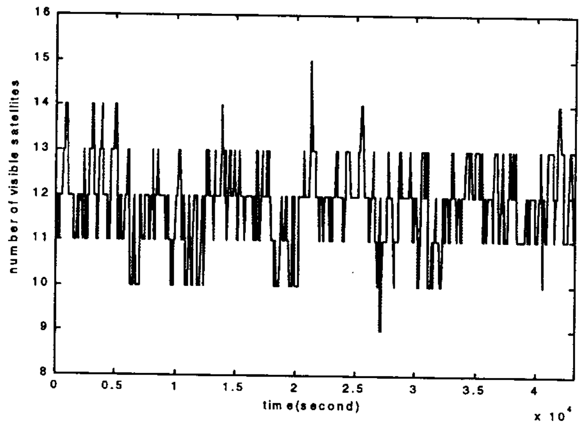

Fig.6 Number of visible GPS satellites

Performance of conventional selection algorithm

Two conventional GPS satellite selection algorithms are discussed as follow.

(a) GDOP is computed for all combinations of four satellites taken from all visible satellites. Then the combination which gives the smallest GDOP is selected.

(b) First, six satellites with the highest elevation angles are selected, then GDOP is computed for all combinations of four satellites from this group of six, and the combination with the smallest GDOP is selected.

Of course the conventional algorithm (a) results in the minimum GDOP, as illustrated in Fig. 7. Therefore this case is used as the reference when comparing the GDOP performance of various selection algorithms. However, the conventional algorithm (a) requires many computations which would be a burden for the GPS receiver. It is an even more serious problem for the GPS receiver onboard space vehicles, since more GPS satellites are visible in space than from land. Considering the minimum number (9) and maximum number (15) of visible GPS satellites illustrated in Fig.6, the number of GDOP computations are 126 and 1365, respectively.

Another disadvantage of the conventional algorithm (a) is that the selected satellites may change frequently from one update to the next. If a selected satellite is not one that is currently being tracked, it takes a period of time to acquire and start tracking the newly selected satellite. A maximum of six satellites can be tracked simultaneously, providing two spare satellites. If one or two of the selected satellites are not being tracked, the spare satellites can be used to form a solution until the new satellites are tracked. However, if three or all four satellites selected are not being tracked, this can lead to a loss of navigation data until at least four satellites can be tracked. Fig.8 illustrates the number of changed satellites between subsequent satellite sets selected by the algorithm (a).

The conventional algorithm (b) has much less computations, where the number of GDOP computations is fixed at 15, and it also shows better continuity performance. However, the GDOP of the algorithm at some points is too large to be acceptable. Figs. 9 and 10 show the GDOP and the number of changed GPS satellites between subsequent satellite sets of the conventional algorithm (b) in the simulation.

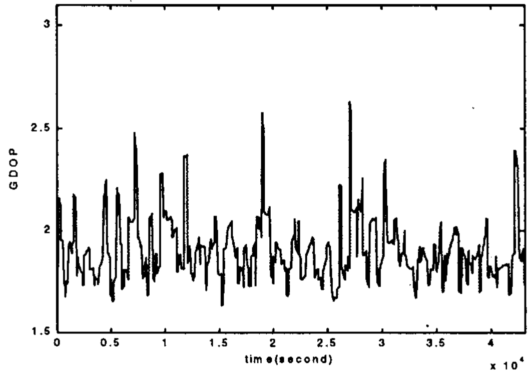

Fig.7 Minimum GDOP of the algorithm (a)

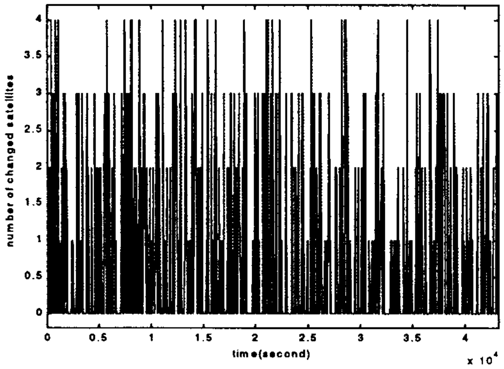

Fig.8 Number of changed satellites of the algorithm (a)

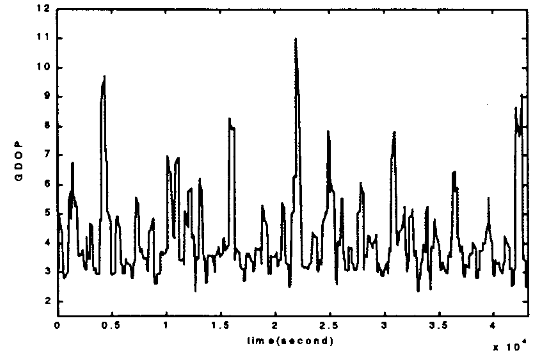

Fig.9 GDOP of the algorithm (b)

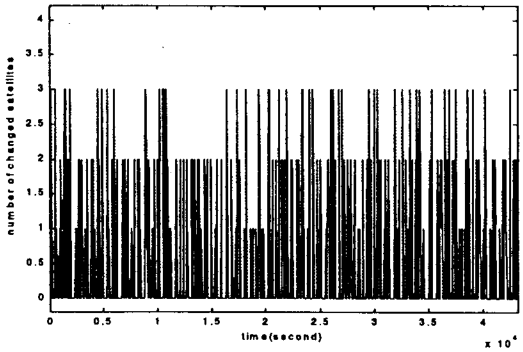

Fig.10 Number of changed satellites of the algorithm (b)

A four-step GPS satellite selection algorithm

This section describes an improved algorithm that has been developed which reduces the number of computations while keeping the GDOP low. Given the components of unit vectors pointing from GP-B to the GPS satellites in the coordinate system $O_I - \vec{X}_I\vec{Y}_I\vec{Z}_I$: e_{1-I}, ... , e_{v-I}, (where v is the number of visible GPS satellites), the four GPS satellites can be selected in the following four steps.

Step1: From all visible satellites select Satellite #1, S1, with the highest elevation angle, or

$$(e_{S1-I})^T e_{GPB-I} = \max_j[(e_{j-I})^T e_{GPB-I}] \qquad (12)$$
$$j = 1, ..., v$$

Step 2: From the remaining visible satellites select S2 with the largest angular distance to S1, or

$$(e_{S2-I})^T e_{S1-I} = \min_j[(e_{j-I})^T e_{S1-I}] \qquad (13)$$
$$j = 1, ..., v \text{ and } j \neq S1$$

Step 3: Based on S1 and S2, a reference triad $\{ e_X, e_Y, e_Z \}$ can be established as

$$e_Z = e_{S1-I} \qquad (14)$$

$$e_Y = (e_{S1-I} \times e_{S2-I}) / |e_{S1-I} \times e_{S2-I}| \qquad (15)$$

$$e_X = e_Y \times e_Z \qquad (16)$$

A regular tetrahedron $\{ R_A, R_B, R_C, R_D \}$ can be defined, whose components of direction vectors of the four vertices in $O_I - \vec{X}_I\vec{Y}_I\vec{Z}_I$ are

$$[V_{RA}\ V_{RB}\ V_{RC}\ V_{RD}] = [e_X\ e_Y\ e_Z] \cdot [V_A\ V_B\ V_C\ V_D] \quad (17)$$

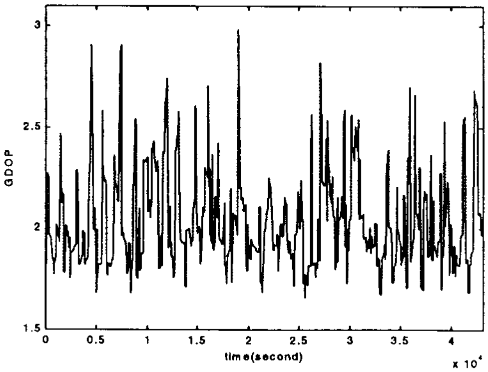

Fig.12 GDOP of the four-step selection algorithm

From the remaining visible satellites S3 is selected which has the smallest angular distance to R_C or R_D, or

$$\begin{aligned} &\max[(e_{S3-I})^T V_{RC}, (e_{S3-I})^T V_{RD}] \\ &= \max_j\{\max[(e_{j-I})^T V_{RC}, (e_{j-I})^T V_{RD}]\} \\ &\qquad j = 1, ..., v \text{ and } j \neq S1, S2 \end{aligned} \qquad (18)$$

Step 4: From the remaining visible satellites S4 is selected to minimize GDOP, or

$$GDOP(S1,S2,S3,S4) = \min_j[GDOP(S1,S2,S3,j)] \quad (19)$$
$$j = 1, ..., v \text{ and } j \neq S1, S2, S3$$

Fig.11 illustrates the four-step procedure of the GPS satellite selection. It is clear that the number of the GDOP computations of the algorithm is less than the number of visible satellites. Fig.12 illustrates GDOP of the four-step GPS satellite selection algorithm, and Fig.13 illustrates the number of changed satellites in subsequent satellite sets.

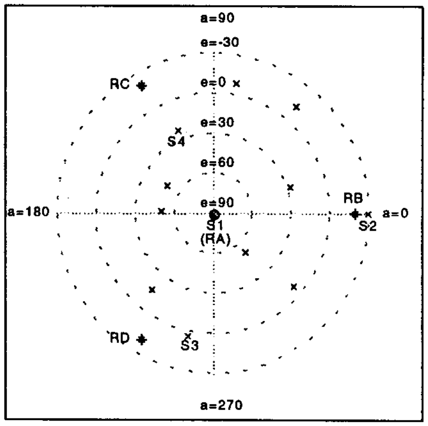

Fig.11 Four-step selection of GPS satellites

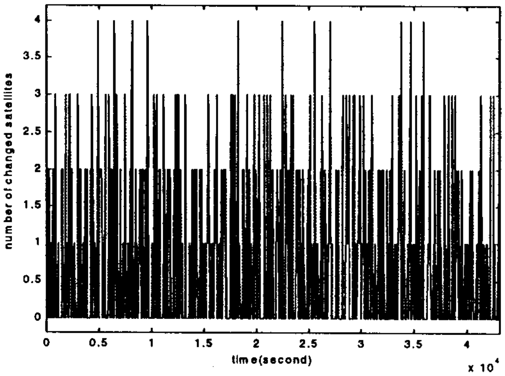

Fig.13 Number of changed satellites of the four-step selection algorithm

GPS satellite selection algorithm with smooth transfer

The selected GPS satellite set is updated periodically. Comparing the subsequent satellite sets, the satellites may be all the same, or one, two, or three satellites may be different. In some cases the four satellites may be totally different. The fewer the number of changed satellites in subsequent sets, the better continuity of the GPS receiver in tracking GPS satellites. In the following discussion an algorithm is presented to make use of the two spare channels for the smooth transfer between subsequent GPS satellite sets so that continuity of navigation data is maintained.

Let the selected set of four satellites at time t_n and t_{n+1} be denoted as

$$G_n = \{S1_n,\ \ S2_n,\ \ S3_n,\ \ S4_n\} \tag{20}$$
$$G_{n+1} = \{S1_{n+1},\ \ S2_{n+1},\ \ S3_{n+1},\ \ S4_{n+1}\} \tag{21}$$

For the smooth transfer from G_n to G_{n+1}, the following 3 cases are considered.

Case 1: Number of changed satellite is 4. An intermediate set $\{S1_{n+1}, S2_{n+1}, B1, B2\}$ is determined, where $B1$, $B2$ are selected from the 4 satellites in G_n to minimize $GDOP\{S1_{n+1}, S2_{n+1}, B1, B2\}$. In this case 6 additional GDOP computations are required. The switch from G_n to G_{n+1} is done as follows: At time t_n four channels are assigned to the four satellites of G_n, and the fifth and sixth channels are assigned to $S1_{n+1}$ and $S2_{n+1}$. When $S1_{n+1}$ and $S2_{n+1}$ are being tracked, the working set is switched to the intermediate set, $S3_{n+1}$ and $S4_{n+1}$ are assigned to the two channels which are used to track satellites other than $B1$ and $B2$ in G_n. When $S3_{n+1}$ and $S4_{n+1}$ are tracked, the working set is switched to G_{n+1}.

Case 2: Number of changed satellites is 3. An intermediate set $\{A0, B1, C1, C2\}$ is also determined in this case, where $A0$ is the only common member in G_n' and G_{n+1}, $B1$ is selected from the remaining 3 satellites in G_n, and $C1$, $C2$ are selected from the remaining 3 satellites in G_{n+1}. $B1$, $C1$, $C2$ are determined to minimize $GDOP\{A0, B1, C1, C2\}$. In this case 9 additional GDOP computations are required. The switch from G_n to G_{n+1} can be done with the intermediate set as in Case 1.

Case 3: Number of changed satellites is less than 3. In this case the two spare channels can be used during the switch from G_n to G_{n+1}, and no additional GDOP computations are required.

Fig.14 illustrates GDOP of the four-step GPS satellite selection algorithm with smooth transfer, and Fig.15 illustrates the GDOP increment compared to the algorithm without smooth transfer. It is shown that the increment of GDOP is generally less than 0.4 when the smooth transfer between subsequent satellite sets is considered. As illustrated, GDOP may decrease in some cases, since the switch through the intermediate set increases the update frequency.

Table 2 compares the performance of the four-step GPS satellite selection algorithm with conventional algorithms in simulations, where the update period is 1 minute. It is shown that the new algorithm presented in this paper has good performance with much less computations. Since the cases where 3 or 4 satellites change in subsequent satellite sets are less than 10%, additional computations for smooth transfer are limited.

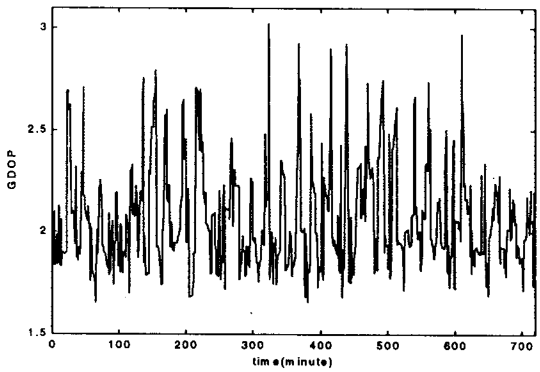

Fig.14 GDOP of the four-step selection algorithm with smooth transfer

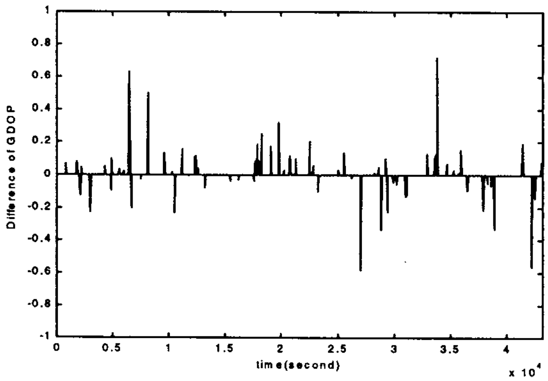

Fig. 15 GDOP increment when the smooth transfer is considered

	GDOP			Statistics in Number of Changed Satellites					Computation
	min	mean	max	4	3	2	1	0	
Conventional Algorithm (a)	1.63	1.90	2.63	30 4.2%	78 10.8%	77 10.7%	68 9.5%	466 64.8%	high
Conventional Algorithm (b)	2.35	4.18	11.03	0 0.0%	47 6.5%	94 13.1%	69 9.6%	509 70.8%	low
Four-Step Selection Algorithm	1.66	2.04	2.98	12 1.7%	59 8.2%	109 15.2%	134 18.6%	405 56.3%	low

Table 2. Comparison of performance of GPS satellite selection algorithms

Performance versus update period

So far we have used a fixed update period of 1 minute. However, 1 minute may be too frequent, and may not permit the receiver to acquire signals on time. Therefore, simulations are carried out to study the performance of the four-step GPS selection algorithm when the update period varies. Figs. 16 and 17 illustrate the number of visible GPS satellites and GDOP of the selection algorithm as a function of update period. It is shown that GDOP doesn't increase very much when the update period is less than 5 minutes. A 5 minute interval results in even lower computation loads.

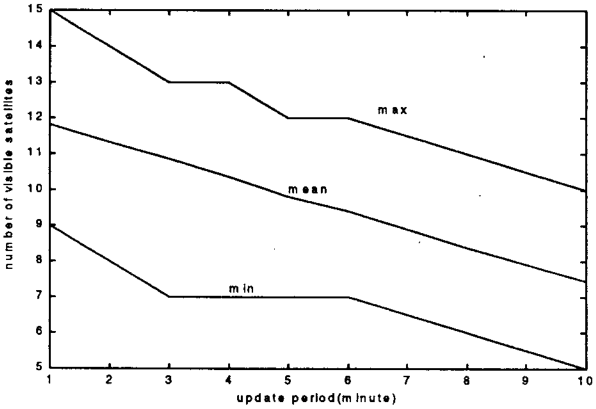

Fig.16 Number of visible satellites versus update period

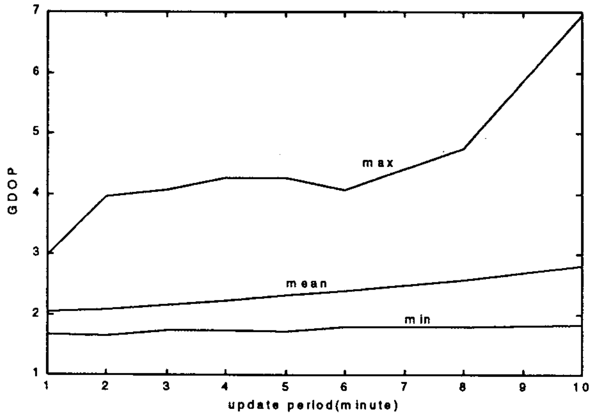

Fig. 17 GDOP versus update period

ANTENNA SELECTION ALGORITHM

While GP-B rolls in the direction of the guide star, the FOV of antennas will also rotate in inertial space. The master antenna has to be transferred among the four antennas to keep tracking a specific GPS satellite. The transfer between two antennas can only be done in the common FOV to prevent tracking discontinuities.

Since the roll period of GP-B is very small compared to the orbit period of GPS satellites, the direction vector of a GPS satellite remains almost fixed in inertial space in a roll period. It traces out a cone in $O_B - \vec{X}_B\vec{Y}_B\vec{Z}_B$, and the body elevation angle (the angle referenced to the plane $O_B - \vec{X}_B\vec{Y}_B$, positive in the direction of $\vec{Z}_B$,) remains constant. Fig.18 shows the areas available for antenna transfer. It is clear that the direction vectors with the body elevation angle of 75°~90° remain in the FOV of antennas 1 or 2 during the roll, those with the angle of -90°~-65° remain in the FOV of antennas 3 or 4, so no antenna transfer is necessary. The direction vectors with the body elevation angle of 30°~75° and -65°~-30° must be transferred between antennas 1-2 and 3-4 respectively, while those with the angle of -30°~30° must be transferred among antennas 1-2-3, 1-2-4, 1-3-4, or 2-3-4. In Fig.18. the parts of the trace which are available for transfer are plotted in the solid line.

The principle of the antenna selection algorithm is to maximize the SNR of the master antenna, which can be realized in the following two ways:

(1) The receiver has measurements of SNR of four antennas, so the master antenna can be assigned autonomously to the antenna with the largest SNR.

(2) The attitude information from the attitude control subsystem of GP-B is used to determine the direction vector of the GPS satellite in $O_B - \vec{X}_B\vec{Y}_B\vec{Z}_B$, and the master antenna is assigned to the antenna in which the GPS satellite has the highest elevation angle.

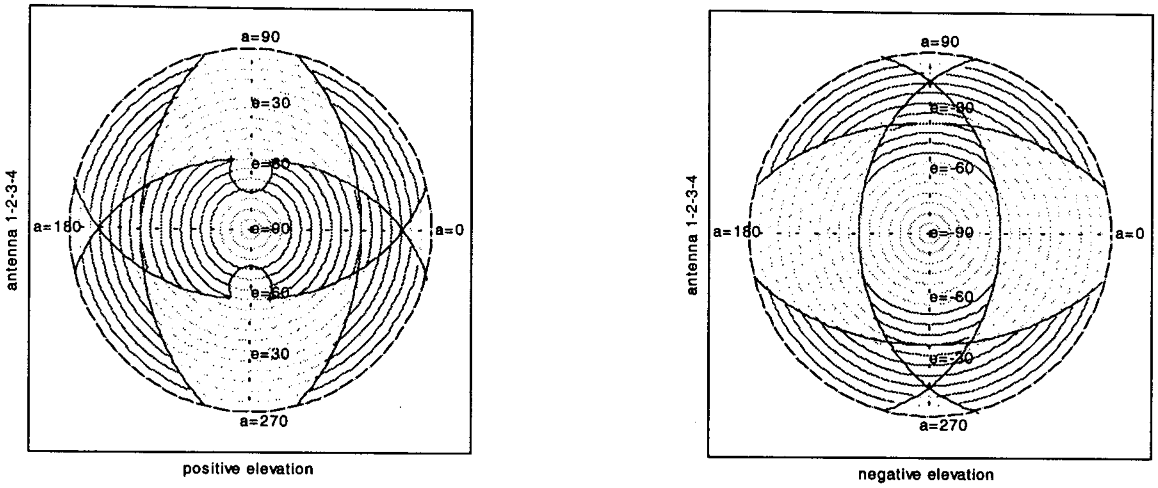

Fig.18 Area available for antenna transfer

Let C_{BI} be the transformation matrix from $O_B - \vec{X}_B\vec{Y}_B\vec{Z}_B$ to $O_I - \vec{X}_I\vec{Y}_I\vec{Z}_I$, the master antenna assigned to track GPS satellite *j* can be determined as

$$(Va_{master-B})^T C_{BI} e_{j-I} = \max_k[(Va_{k-B})^T C_{BI} e_{j-I}] \qquad (22)$$

k=1, 2, 3, 4.

CONCLUSIONS

The GPS receiver satellite/antenna selection algorithm for the Stanford Gravity Probe B Relativity Mission is discussed in this paper, which determines the visibility of GPS satellites and assigns a GPS satellite and a master antenna to each channel of the GPS receiver to maintain signal tracking. The general purpose of the GPS satellite selection algorithm is to minimize GDOP to improve the position accuracy. However, minimum GDOP algorithms tend to be computationally intensive, and some computationally simpler algorithms have poor GDOP performance. In this paper a four-step GPS satellite selection algorithm is presented, which shows good performance with much less computations compared to conventional algorithms. The smooth transfer between subsequent GPS satellite sets is also considered, such that continuity of the navigation data is maintained. The antenna selection algorithm is designed to maximize the SNR of the master antenna. Simulation results demonstrate the good performance of the new algorithm presented in this paper.

ACKNOWLEDGMENTS

Gratitude is acknowledged to NASA for supporting this research under Contract No. NAS8-39225. Trimble Navigation Ltd. is gratefully acknowledged for its support. The authors would also like to thank Lockheed Martin Missiles and Space for their support, especially Jason Suchman for supplying antenna visibility information. Thanks also goes to Dr. Hirohiko Uematsu of NASDA for providing the spacecraft diagram shown in Figure 1.

REFERENCES

1. C.W.F.Everitt, "The Stanford Relativity Gyroscope Experiment(A): History and Overview", in *Near Zero: New Frontiers of Physics*, J.D.Fairbank, J.B.S.Deaver, C.W.F.Everitt, P.F.Michelson, Eds., W.H.Freeman and Company, New York, 1988, pp.587-639.
2. H.Uematsu, B.W.Pakinson and E.G.Lightsey, "GPS Receiver Design and Requirement Analysis for the Stanford Gravity Probe B Relativity Mission", *Proceedings of ION GPS-95*, The Institute of Navigation, Palm Springs, California, Sept. 12-15, 1995, pp.237-246.
3. H.Uematsu and B.W.Parkinson, "GPS Receiver Development and Verification Tests for Stanford Gravity Probe B Relativity Mission: Verification Test Plan and Preliminary Results", *Proceedings of ION GPS-96*, The Institute of Navigation, Kansas City, Missouri, Sept. 17-20, 1996, pp.1377-1385.
4. J.J.Spilker, "Satellite Constellation and Geometric Dilution of Precision", in *Global Positioning System: Theory and Applications, Vol. I*, B.W.Parkinson and J.J.Spilker Eds., AIAA, Inc., 1996, pp.177-208.
5. M.Kihara and T.Okada, "A Satellite Selection Method and Accuracy for the Global Positioning System", *Navigation*, Vol.31, No.1, 1984, pp.8-20.